[
Draft version July 27, 2021
Typeset using LaTeX **preprint2** style in AASTeX63

Presolar grain isotopic ratios as constraints to nuclear and stellar parameters of AGB nucleosynthesis

Sara Palmerini,[1,2] Maurizio Busso,[1,2] Diego Vescovi,[3,2] Eugenia Naselli,[4] Angelo Pidatella,[4] Riccardo Mucciola,[1,2] Sergio Cristallo,[5,2] David Mascali,[4] Alberto Mengoni,[6,7] Stefano Simonucci,[8,2] and Simone Taioli[9,10,11]

[1]*Department of Physics and Geology, University of Perugia, Via A. Pascoli snc, I-06123 Perugia, Italy*
[2]*INFN, section of Perugia, Via A. Pascoli snc, I-06123 Perugia, Italy*
[3]*Goethe University Frankfurt, Max-von-Laue-Strasse 1, Frankfurt am Main 60438, Germany;*
[4]*INFN, Laboratori Nazionali del Sud, Via S. Sofia, I-95129 Catania, Italy*
[5]*INAF, Osservatorio Astronomico d'Abruzzo, Via Mentore Maggini snc, I-64100 Collurania, Teramo, Italy*
[6]*ENEA, Agenzia Nazionale per la nuove Tecnologie, l'Energia e lo Sviluppo Economico Sostenibile, Via Martiri di Monte Sole 4, I-40129 Bologna , Italy*
[7]*INFN, Istituto Nazionale di Fisica Nucleare, Sezione di Bologna, Viale Berti Pichat 6/2, I-40127 Bologna, Italy*
[8]*Physics Division, School of Science and Technology, University of Camerino, Via Madonna delle Carceri 9B, I-62032 Camerino, Macerata, Italy*
[9]*European Centre for Theoretical Studies in Nuclear Physics and Related Areas, Str. delle Tabarelle, 286, 38123 Villazzano, Trento, Italy*
[10]*Trento Institute for Fundamental Physics and Applications, Via Sommarive, 14, 38123 Povo ,Trento, Italy*
[11]*Peter the Great St. Petersburg Polytechnic University, Russia*

(Received; Revised; Accepted)

Submitted to ApJ

ABSTRACT

Recent models for evolved Low Mass Stars (with $M \lesssim 3$ M$_\odot$), undergoing the AGB phase assume that magnetic flux-tube buoyancy drives the formation of ^{13}C reservoirs in He-rich layers. We illustrate their crucial properties, showing how the low abundance of ^{13}C generated below the convective envelope hampers the formation of primary ^{14}N and the ensuing synthesis of intermediate-mass nuclei, like ^{19}F and ^{22}Ne. In the mentioned models, their production is therefore of a purely secondary nature. Shortage of primary ^{22}Ne has also important effects in reducing the neutron density. Another property concerns AGB winds, which are likely to preserve C-rich subcomponents, isolated by magnetic tension, even when the envelope composition is O-rich. Conditions for the formation of C-rich compounds are therefore found in stages earlier than previously envisaged. These issues, together with the uncertainties related to several nuclear physics quantities, are discussed in the light of the isotopic admixtures of s-process elements in presolar SiC grains of stellar origin, which provide important and precise constraints to the otherwise uncertain parameters. By comparing nucleosynthesis results with measured SiC data, it is argued that such a detailed series of constraints indicates the need for

Corresponding author: Sara Palmerini
sara.palmerini@unipg.it, sara.palmerini@pg.infn.it

new measurements of weak interaction rates in ionized plasmas, as well as of neutron-capture cross sections, especially near the N = 50 and N = 82 neutron magic numbers. Nontheless, the peculiarity of our models allows us to achieve fits to the presolar grain data of a quality so far never obtained in previously published attempts.

Keywords: Nuclear Astrophysics — Nucleosynthesis, *s*-process — Stellar weak interactions — Stars, evolution — Stars, abundances

1. INTRODUCTION.

Several attempts are currently made in the literature for inferring which mixing mechanisms be responsible for the formation of ^{13}C reservoirs in He-rich layers below the convective envelopes of evolved stars. These reservoirs have been proven to be present in stars ascending for the second time the Red Giant Branch, called Asymptotic Giant Branch stars (hereafter AGB, see e.g. Busso et al. 1999; Herwig 2005; Straniero et al. 2006). The availability of freshly produced ^{13}C concentrations is there crucial to understand the production of neutron-rich elements observed in their photospheres (Abia et al. 2003, 2020) as well as to account for the enrichment of heavy elements beyond Sr in the Galaxy (Maiorca et al. 2011, 2012; Magrini et al. 2021), especially those belonging to the so-called *main component* of the slow neutron-capture process, i.e. the *s-process* (Käppeler et al. 2011). Among the mentioned attempts, recent publications (Vescovi et al. 2020; Busso et al. 2021) underlined the relevance of Magnetohydrodynamics(MHD)-based mixing schemes, made possible by the peculiar physics prevailing below the convective envelopes (Nordhaus et al. 2008; Nucci & Busso 2014), especially during the repeated downward penetrations of their convective envelopes, collectively indicated as the *Third Dredge-Up* (hereafter TDU, Karakas & Lattanzio 2014), which mix freshly produced elements to the surface. In this note, we want to discuss some properties of the above models that immediately affect the ensuing nuclear yields for heavy nuclei. These topics will be analyzed, in conjunction with relevant issues concerning the nuclear input parameters (cross sections and weak-interaction rates), using as a test-bench the requirement of reproducing isotopic ratios of heavy elements measured in presolar SiC grains (Zinner 2014; Lugaro et al. 2018). We intend to show that, in order to account for the observations and to decide among different model possibilities, we need a better assessment of neutron-capture cross sections near magic neutron numbers as well as new experimental data on β-decay rates in ionized plasmas. In order to demonstrate the above issues, in section 2 we illustrate some peculiar properties of recent models for evolved low-mass stars, while in section 3 we discuss nuclear input parameters relevant for the synthesis of neutron-rich nuclei in the mentioned atomic mass region. Section 4 then discusses the improvements possible today in the treatment of weak interactions. In particular, using as a guiding example the case of ^{134}Cs, we show briefly the requirements for nucleosynthesis models, as well as what can be obtained by modern theoretical approaches and what will be soon available in the field of experimental verifications, through the project PANDORA (Mascali et al. 2017, 2020). Subsequently, in section 5, we briefly outline the experimental database of presolar SiC grain measurements and then in section 6 we discuss how the model results compare with these detailed constraints, examining the most important evidence emerging from the comparison. Preliminary conclusions from this work are then drawn in section 7.

2. RELEVANT PROPERTIES OF THE ADOPTED STELLAR MODELS.

2.1. *Stellar layers hosting neutron captures*

It is known since many years (Harris et al. 1985; Gilroy & Brown 1991) that the isotopic abundances shown by red giant photospheres can be accounted for only if non convective mixing mechanisms below the envelope are at play. Their nature has been an important object of research in stellar physics over the past decades (see e.g. Wasserburg et al. 1995; Langer et al. 1999; Herwig et al. 2003; Denissenkov & VandenBerg 2003; Denissenkov & Tout 2003; Eggleton et al. 2006, 2008; Cristallo et al. 2009a; Charbonnel & Lagarde 2010; Busso et al. 2010; Nucci & Busso 2014; Cristallo et al. 2018, and references therein). Some of these mechanisms must operate also below the TDU in AGB stars, in order to let protons from the envelope be mixed into the He-rich layers. They will subsequently produce ^{13}C at H-burning reactivation and then neutrons thanks to the ^{13}C(α,n)^{16}O reaction (Arlandini et al. 1999; Busso et al. 2001; Cristallo et al. 2009b,a; Bisterzo et al. 2012; Trippella et al. 2014). Later on (several 10^4 yr later, in stars below about 3 $M_\odot$), a thermal instability occurs (*Thermal Pulse, or TP*) in the He shell that lays at the bottom of the He-rich zone below the convective envelope. This instability is due to the combined effects of the gradual compression of these layers, operated by H-shell burning, by the degeneracy of the C-O core and by the natural difficulty of maintaining stability in a thin burning shell (Yoon et al. 2004). An intermediate convective buffer then fills the He-rich region, while the temperature increases rapidly. For low-mass stars ($1 \lesssim M/M_\odot \lesssim 3$) this growth does not achieve values significantly larger than $T \simeq 3{\cdot}10^8$K, but in more massive red giants it can lead to quite higher temperatures (above $3.5 \cdot 10^8$K). Then the complementary neutron source ^{22}Ne(α,n)^{25}Mg can be activated: it is restricted at rather high temperature regimes because its Q value is negative ($Q_{22}^{(\alpha,n)}$ = -478 keV, see e.g. Soppera et al. 2011; Adsley et al. 2021). Hence, in low-mass stars (where, as said, $T \lesssim 3 \cdot 10^8$ K) its effects are not large: they mainly control the freeze-out of reaction branchings for which nuclear parameters depend on T. The cycle of ^{13}C(α,n)^{16}O and ^{22}Ne(α,n)^{25}Mg activation is repeated several times in AGB stars: actually, repeated exposures are known since decades to be required to feed adequately the whole distribution from Fe to Pb (Seeger et al. 1965; Kaeppeler et al. 1990a).

In the framework outlined above, previous MHD models for mass circulation in evolved stars (Busso et al. 2007; Nucci & Busso 2014; Trippella et al. 2016; Palmerini et al. 2018) have been applied recently (Vescovi et al. 2020; Busso et al. 2021) to the production of ^{13}C and then of neutron-rich elements beyond Fe through slow neutron captures. The basic properties of those recent computations can be understood with reference to Figures 1 and 2. The first one illustrates the occurrence of a TDU episode, with the underlying layers that must be affected by extra-mixing, while the second shows the peculiar distribution of protons (and later of ^{13}C and ^{14}N) ensuing from this specific mixing scheme. Extensive discussions of the computations that lay behind the formation of reservoirs similar to the one of Figure 2 were presented in the above mentioned works.

As Figure 2 shows, the new distribution has some peculiar characteristics. Namely, the abundance of protons remains always very low; so low, actually, that H burning cannot efficiently proceed to ^{14}N, because it is consumed almost completely by the ^{13}C production. This is so everywhere, except in a thin top layer where ^{13}C is abundant. By comparison, a purely exponential distribution is shown in Figure 2 (see panel *a*). It presents a rather wide layer in mass where protons are sufficiently abundant

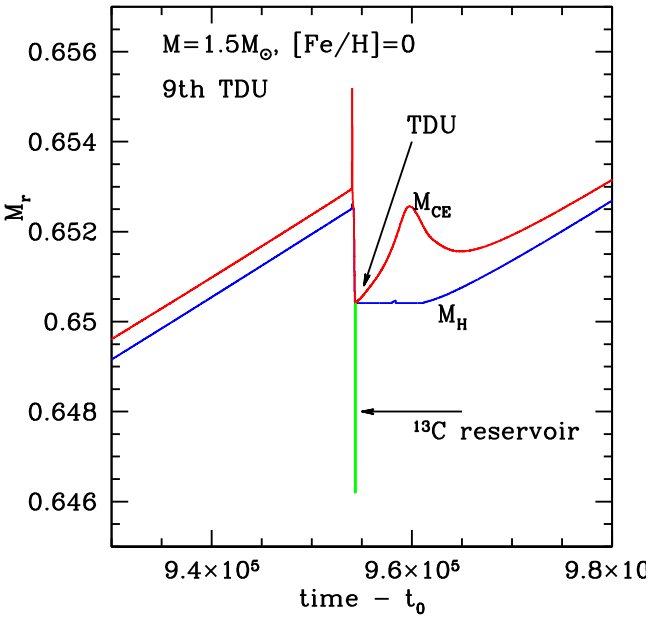

Figure 1. The occurrence of the envelope penetration in a Third Dredge Up episode, for a mass M=1.5 $M_\odot$ of solar metallicity. The figure shows in red the innermost border of the convective envelope ($M_{\rm CE}$) and in blue the position of the H/He interface ($M_{\rm H}$). Its minimum before H-burning restarts is called *post-flash dip*. The parameter t_0 is the stellar age at the moment of the first TDU episode. Note how, of the rather long duration of the post-flash dip ($\sim 10^4$ yr), only a short fraction (about a century) is really occupied by TDU. The ^{13}C pocket (here extending for 4.2x10^{-3} $M_\odot$) is represented in green. Its structure, as well as that of the previous H-rich pocket, are expanded in Figure 2.

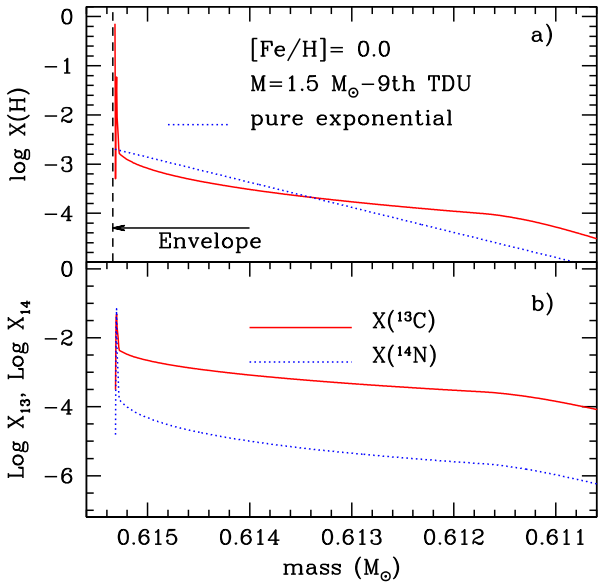

Figure 2. The abundances in the ^{13}C pocket at the TDU represented in Figure 1. Panel *a* shows the profile of the proton abundance, penetrated according to equations from (14) to (17) by Trippella et al. (2016), as computed in Busso et al. (2021). Panel *b* shows the ensuing abundances of ^{13}C and ^{14}N formed after hydrogen burning in the shell restarts. Later, in these layers the ^{13}C(α,n)^{16}O reaction will release neutrons for $s-$processing.

to synthesize considerable ^{14}N concentrations. Since ^{14}N is an efficient *poison*, or neutron-absorber, the number of neutrons available for being captured by ^{56}Fe and its progeny is enhanced in our new models and so is the neutron exposure per cycle, in the various pulse-interpulse cycles mentioned for AGB stars.

By contrast, in our computations the shortage of ^{14}N cuts drastically the nuclear channels starting from nitrogen, thus reducing the production of several isotopes in the mass range 15-30, including ^{18}O, ^{19}F and ^{22}Ne. The reduced production of this latter, in particular, hampers the efficiency of the ^{22}Ne(α,n)^{25}Mg source in the *TP*s, leading to a type of *s*-processing never achieving high neutron densities, hence feeding only marginally nuclei at the neutron-rich side of crucial branching points of the *s*-process, like ^{86}Kr, ^{87}Rb, ^{96}Zr, etc., even during the neutron flows available in the convective buffers accompanying *TP*s. Another consequence of the reduced ^{14}N abundance is that the production of ^{19}F is inhibited sharply, which fact promises to account well for its low abundance in AGB photospheres (Abia et al. 2015, 2019). This last point deserves a closer scrutiny, which goes beyond the scopes of this note and is presented by Vescovi, D. et al. (2021).

2.2. *Magnetic effects in stellar winds*

Our mixing scheme was originally built from an analogy based on the physics of magnetic flux tubes in the Sun (Busso et al. 2007). Solar magnetic structures cross the convective layer emerging from the regions in the tachocline where the dynamo mechanism has its roots and a similar behavior can be at least partially envisaged in evolved stars (Ayres et al. 1981). A substantial difference lies in the fact that stars of classes IV, III and II, with spectral types later than K3 stay, in the Hertzsprung-Russell diagram, at the cool side of the so-called *Coronal Dividing Line*, or CDL (Linsky & Haisch 1979), i.e. of the border separating bluer, X-ray emitting active stars (where high-energy radiation is due to charged particles trapped in coronal loops) from redder giants not displaying evidence of a magnetized corona in space-borne X-ray observations (Haisch et al. 1991). Following Holzwarth & Schüssler (2001), the dividing line can actually be seen as a border beyond which the large convective envelopes tend to trap the buoyant flux tubes, generally hampering their outward emergence in a corona.

The above scenario is largely accepted; for our purposes, trapping and breaking of magnetic flux tubes in the envelope guarantees the mixing of nucleosynthesis products (Trippella et al. 2016; Vescovi et al. 2020; Busso et al. 2021).

Despite the lack of a real corona as a large-scale structure, observations of magnetic fields at the surface of AGB stars are numerous (see e.g. reviews by Vlemmings 2011, 2012, and references therein). In particular, Jordan et al. (2005) reported field values of the order of a kilogauss in central stars of Planetary Nebulae (PNe), while fields of lower intensity (up to 10 G) were observed through VLBI techniques since the nineties (Kemball & Diamond 1997). More recently, Herpin et al. (2006, 2007) reported measurements of the magnetic Zeeman effect on SiO masers at 2-10 AU from the central stars, suggesting that the corresponding fields act as catalysts for dust formation and as collimators for the winds. Fields of similar intensity (from 0.6 to 10 G) were observed around C-rich evolved stars (Duthu et al. 2017) and post-AGB objects (Sabin et al. 2015a,b).

MHD models of a dynamo effect in AGB stars and of its consequences on mass outflows were performed by Pascoli & Lahoche (2008, 2010); Pascoli (2020). They suggest that, from the point of view of a distant observer, the nebula generated around an AGB star would not show signs of deformation from a spherical shape up to and through the slow superwind phase. By contrast, anisotropic structures would be already developing, induced by magnetic sources; these ones would remain hidden in the innermost regions, creating a bipolar cavity during the early superwind phases. Then, the pre-PNe stage would begin when the fast wind emitted by the core engulfs this cavity and increases the anisotropy of the gas distribution.

The development of anisotropic structures was early suggested by Rosner et al. (1991, 1995), who assumed a change in the topology of the atmospheric magnetic field from large, coherent coronal loops (that would appear at the hot side of the CDL) to an open field-line geometry where only small loops would remain (so that the star would move to the cool side of the CDL). The larger surface fraction covered by open field lines would then allow for the escape of a cool, massive stellar wind driven by Alfvén waves. Among subsequent suggestions of persisting links between magnetic activity and AGB winds, one has to mention the work by Soker & Kastner (2003). According to them, magnetic flares can occur in AGB stars, above photospheric cool regions similar to solar dark spots. Their presence would enhance locally both the wind efficiency and the dust formation. Another important confirmation on the presence of magnetic fields in low mass stars comes from recent white dwarf (WDs) stud-

ies. Magnetism in WDs is determined via polarization measurements and the observation of characteristic distortions and shifts of spectral lines due to the Zeeman effects. In the past, the estimated frequency of the occurrence of magnetic fields in WDs was rather low, because it was mainly based on discoveries made with low resolution classification spectroscopy, which is mainly sensitive to field strength between 1 and 100 MG. In recent years, new high-resolution spectroscopic and spectropolarimetric measurements have shown that at least 20% of WDs host magnetic fields, with typical strengths from a few kG up to about 1000 MG. Recently, Bagnulo & Landstreet (2020) discovered a significant number of new WDs with strong magnetic fields (from 5 to 200 MG strength) in the 20 pc volume around the solar system, highlighting again the importance of spectropolarimetry in detecting magnetic fields in these compact objects. This result is in agreement with previous suggestions (Aznar Cuadrado et al. 2004; Kawka & Vennes 2014), confirming the suspicion that magnetism is more a common than a rare characteristic of WDs.

For the purposes of this work, we can then recognize that there is ample support in the literature to the existence of open magnetic structures at the AGB surface (relics of the original flux tubes survived to turbulence in the convective layers) where dust formation can occur and even become very efficient. This possibility is broadly in line with the present picture of AGB mass loss, where the traditional idea of a rate steadily increasing with time, up to the final superwind stages where most of the mass would be lost, has been substituted by a very complex scenario, characterized by a non-monotonic growth of the wind efficiency, affected by pulsation and other dynamical phenomena and in which the total mass ejected in final hot superwind stages is possibly reduced by their rather short duration (see e.g. Höfner & Olofsson 2018, for an updated review)

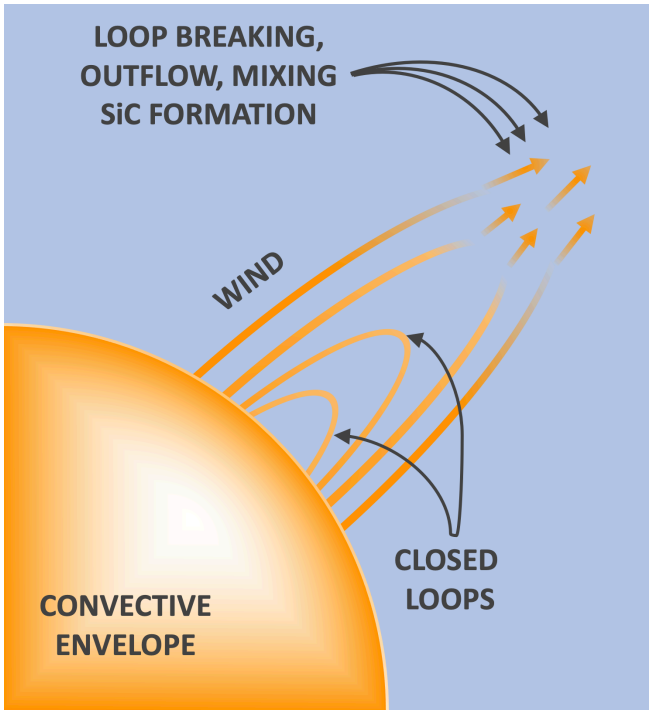

Figure 3. A cartoon representing schematically the breaking of magnetic structures in the stellar winds (e.g. coronal flux tubes, carrying C-rich matter and *s*-process nuclei).

In our approach, among the dynamical phenomena affecting the winds in the TDU phase there would be the formation of regions in which a few magnetic structures, carrying C-rich material outward, would ultimately open, accompanying and possibly guiding gaseous and dusty winds. A schematic representation of this phenomenon is shown as a cartoon in Figure 3.

The above scenario offers an important tool to the comparison of model results with observations. In particular, C-rich structures, breaking within the wind and mixing there with the ambient composition, would be present at any mo-

ment in the evolution of an AGB star. As the material they transport from the He-shell regions is very largely enriched in carbon (about 25% of abundance in mass) tiny traces of it remaining in the wind would be sufficient to permit formation of blobs with a C/O ratio exceeding unity, so that carbon-based dust like SiC can form, even when the general composition of the envelope is O-rich.

In order to account for the above possibility, in section 6 and in the accompanying figures we shall compare the isotopic composition measured in presolar SiC grains both with model envelope abundances and with those of a phase (called *magnetic wind*, or *MW*) obtained by mixing the envelope with a limited percentage (from 0.5% to 5%) of material having the He-shell composition most recently transported outward by flux tubes. This would mimic the effects of magnetic flares or of other instabilities breaking the originally closed loops into open wind structures. A preliminary version of this idea was presented earlier, in a simplified form, by Busso et al. (2021), where the composition of this C-rich wind phase was roughly approximated through the so-called *G-component* of the *s*-processed material (Zinner 1998).

3. STATUS OF THE SET OF NUCLEAR PARAMETERS ADOPTED

As mentioned, detailed information on the isotopic admixture of *s*-processed materials entering the winds of AGB stars and forming dust there are contained in the record of presolar SiC grains, especially of the *Main-Stream* group. From there we can infer relevant constraints on the nuclear parameters controlling stellar neutron captures, especially for nuclei near the magic neutron numbers $N = 50$ and $N = 82$. Recent measurements for them can be found in the updates of the presolar grain database at the Washington University of Saint Louis (Hynes & Gyngard 2009; Stephan et al. 2020). We shall therefore use the most recent sets of data from this repository in order to try an iterative process for improving our knowledge of the nuclear physics that lays behind *s*-processing. We start describing here below the status of the nuclear inputs adopted from the literature, in the aim of finding required and possible improvements.

Except for special cases, mentioned when necessary, Maxwellian-averaged neutron-capture cross sections (MACS) are taken from the KADONIS on-line repository, in its version 1.0 (hereafter K1, see Dillmann et al. 2014, and the KADONIS webpage[1]), whose recommended values are in any case compared with those proposed by the *National Nuclear Data Center* of the *Brookhaven National Laboratory*[2] (Pritychenko & Mughabghab 2012). Choices from this repository will be indicated briefly as coming from *BNL*. When pertinent, the K1 repository presents recommended values that derive from theoretical calculations of the energy dependence, normalized to an actually measured value. They are computed as an average over recent compilations, among which one must cite *ENDF/B-7.1* (Chadwick et al. 2011), *TENDL15*[3], *JEFF3.2*[4] and *JENDL4.0* (Shibata et al. 2011). When renormalizations to gold are necessary, the suggestions by Massimi et al. (2010) and Lederer et al. (2011) are adopted. All the recent measurements from the n_TOF collaboration are also included. For unstable nuclei not present in the K1 repository we used theoretical Hauser-Feshbach computations from the TALYS package[5], in its 2008 version, as discussed by Goriely et al. (2008). Corrections for stellar conditions of the cross sections were introduced using the traditional *Stellar Enhancement Factors* (*SEF*), instead of the recently sug-

[1] https://exp-astro.de/kadonis1.0/
[2] https://www.nndc.bnl.gov/astro/
[3] https://tendl.web.psi.ch/tendl_2015/tendl2015.html
[4] http://www.oecd-nea.org/dbforms/data/eva/-evatapes/jeff_32/
[5] https://tendl.web.psi.ch/tendl_2019/talys.html

gested X-factors from Rauscher (2012). Reasons for this have been discussed in some detail in Busso et al. (2021). Rates for weak interactions as a function of temperature and density are assumed from the work by Takahashi & Yokoi (1987). The ensemble of the above choices will be indicated as our *standard* (ST) case.

For various nuclei discussed in this work considerable uncertainties are still present and are outlined in what follows. In the aim of clarifying some crucial points of the *s*-process path for which new measurements would be important, we shall consider a series of possible local modifications to the input data, as suggested by the comparison with either the presolar grain data or the average solar-system inventory of purely-*s*-process isotopes. The results of computations made using sets of parameters modified ad-hoc to improve the fit to experimental SiC data will be referred to as models of *version 2* (V2).

3.1. *The branching points at ^{84}Kr and ^{85}Kr*

Several nuclei, produced by neutron captures near the magic neutron number $N = 50$ depend more or less remarkably on the operation of the crucial branching points of the *s*-process chain at ^{85}Kr and at its parent ^{84}Kr (see Figure 4 and e.g. the paper by Walter et al. 1986). A recent discussion of this and other branching points on the *main component* in the light of parameterized AGB models was presented by Bisterzo et al. (2015). In the K1 repository the 30 keV recommended cross section for ^{84}Kr is 33.1 mb. This compares very well with the data listed in the *BNL* site, being close to a sort of average of them. The channel pointing to the isomeric state of ^{85}Kr has a branching ratio of 0.586, which means that almost 60% of the flux goes to the isomer (^{85}Kr^m, at 305 keV and with $t_{1/2} \simeq 4.5$h). This estimate is in line with more recent evaluations by Tessler et al. (2021, submitted); it is however higher than in previous standard choices; e.g., in the previous release of KADONIS (v0.3, or K03, Dillmann et al. 2006), where this branching ratio was suggested to be about 40%. Concerning the unstable ^{85}Kr, its ground state has a half-life of about 10.5 yr, sufficient to effectively capture neutrons before the decay, in stellar conditions. Its cross section has only a theoretical estimate and is affected by a high uncertainty (of the order of 50%, typically). The K1 recommended value (73 $\pm$ 34 mb) represents again a sort of average of those reported in the *BNL* repository. A further clarification of all these points is vital, because the flow through the isomeric state subsequently feeds primarily (at 80%) the channel passing through ^{85,86}Rb and then ending up at ^{86,87}Sr, at the expense of ^{86}Kr and ^{87}Rb, which feed only ^{88}Sr. This implies that the ratio of Sr isotopes shown by presolar grains depends not only on their own cross sections, but also on those of ^{84,85}Kr, on the branching ratio to ^{85}Kr^m and on the decay rates of unstable isotopes through which the flow passes (like ^{85}Kr^m itself and ^{86}Rb). New cross section measurements in this mass region would be important also for the understanding of the Rb/Sr ratio in AGB stars and their relatives (see e.g. Roriz et al. 2020, and references therein). With new facilities for measuring weak interactions in ionized plasmas only a couple of years from finalization, it will certainly be worth fixing all these issues on experimental grounds.

3.2. *Sr*

The precise values for the cross sections of the Sr isotopes that are fed by slow neutron captures (^{86}Sr, ^{87}Sr, ^{88}Sr) are crucial for interpreting the isotopic admixtures of Sr itself, as well as their ratios to Ba isotopes, as measured in presolar grains (Liu et al. 2014, 2015, 2018; Stephan et al. 2018). For ^{86}Sr, the 30 keV recommended value is 60 mb, again in good agreement with the *BNL* data and only slightly lower than the previous choice (64 mb) made by K03.

For ^{87}Sr, the recommended value is from experimental measurements (Bauer et al. 1991)

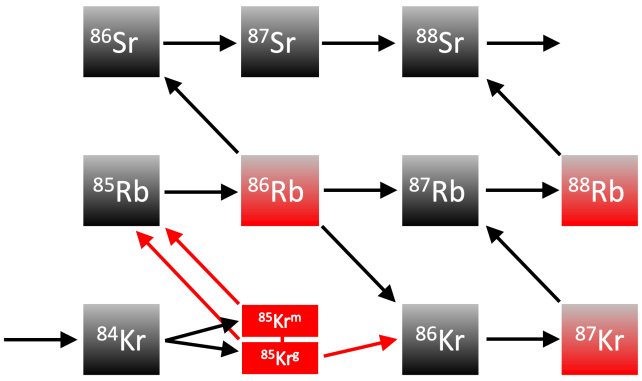

Figure 4. The s-process nucleosynthesis path in the region around $N = 50$; the ^{85}Kr branching is highlighted by the red arrows. Stable isotopes are shown in black boxes while unstable ones have a red background.

and the energy dependence is derived from the repositories mentioned above. The choice by K1 (93.8±3.8 mb) is again only slightly smaller than the one of the previous K03 compilation and compatible (somewhat in the higher part of the distribution) with *BNL* data.

For ^{88}Sr, K1 recommends a re-normalization of previous weighted averages, from measurements such as those by Koehler et al. (2000); Kaeppeler et al. (1990b). However, the presence of discrepancies in the published data from the *Time of Flight* (TOF) and *Activation* methods is noticed and this is a special case in which new experimental efforts are needed. In this respect, we notice that in the most recent measurements by Katabuchi et al. (2011), the 30 keV reference value (9.4 mb) is much larger than recommended by K1 (6.3 mb). This last datum is then slightly larger than most of those from *BNL* (that group around 5.2 mb). This is important especially if considered together with the uncertainties already discussed, affecting the previous branching points of the *s*-chain at ^{84,85}Kr (see above). One can in particular notice that very similar relative production factors for the isotopes of Sr can be obtained in two different ways; namely: (i) by adopting, in neutron captures on ^{84}Kr, the lower value of the branching ratio to ^{85}Kr^m (40%) and taking the neutron capture cross section of ^{88}Sr from the K1 recommendations; or (ii) adopting the higher branching ratio to ^{85}Kr^m (60%), but then using, for the cross section of ^{88}Sr, the measurements by Katabuchi et al. (2011). Our standard choice here will be that of choosing the K1 recommendations, however one has to remember that a lower production of ^{88}Sr is possible using either of the previously mentioned choices (whose effects are mimicked in our case V2). It is clear that on these issues an experimental clarification is urgent, as is a proper treatment of the decay rates of ^{85}Kr and ^{86}Rb in ionized plasmas.

3.3. *Zr and Nb*

An analysis of the possible uncertainties affecting the reproduction of Zr isotopes in SiC grains was early presented by Lugaro et al. (2003), to which we refer the reader for a general assessment of the problem. In our work, for stable Zr isotopes and for the rather long-lived ^{93}Zr, the K1 recommended cross sections include the measurements of the n_TOF collaboration (Tagliente et al. 2008a,b, 2010, 2011a,b, 2013). In particular, the values provided for MACS from 5 to 25 keV were recalculated and normalized to the experimental data at 25 keV. For the unstable ^{95}Zr MACS from 5 keV to 100 keV are from theoretical calculations. Uncertainties are indicated to be between 25 and 50%. The data reported by *BNL* are on average larger by 30% (these choices would produce a larger amount of ^{96}Zr and a lower contribution to ^{95}Mo. We shall mimic this behavior in our cases V2 by using there the K1 cross section at the upper limit of its reported error bar).

From ^{93}Zr an interesting reaction branching departs, based on its β^- decay (early recognized by Bahcall 1962, who indicated it as a source of information on the stellar physical conditions). This decay leads to ^{93}Nb via two

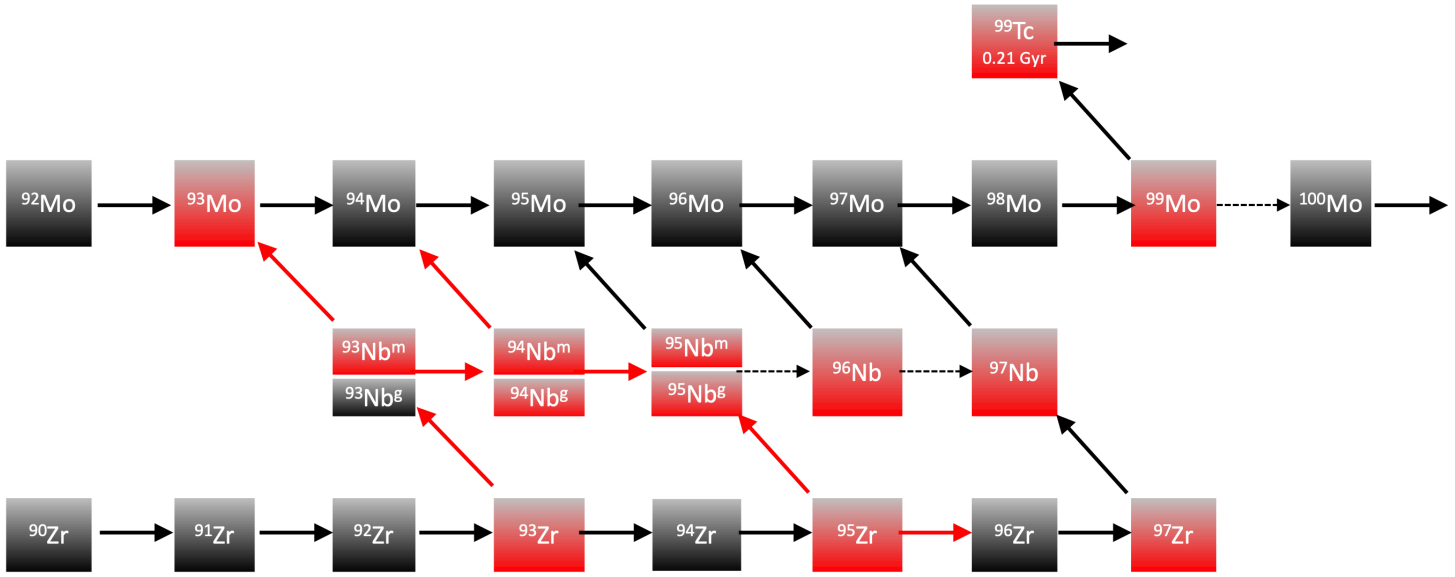

Figure 5. The s-process nucleosynthesis path trough Zr, Nb and Mo isotope. Same color code as in Figure 4.

channels, feeding directly the ground state (with 27% probability) or passing through its isomer ^{93}Nb^{m} (73% probably). The resulting half-life is reported in the *ENSDF* tables[6] to be 1.6·10^{6} yr, hence of the same order as the whole duration of the TP-AGB phase. The ^{93}Nb half-life does not decrease with T below about $4 \cdot 10^{8}$, according to Takahashi & Yokoi (1987). During the development of *TP*s, the temperature quickly increases up to 280-300 MK, where ^{93}Zr is strongly produced, so that at the end of the AGB phase its abundance is between one fourth and one half of those for the nearby nuclei (^{92}Zr and ^{94}Zr). Due to its long half-life, this isotope behaves almost as a stable species during s-processing and ^{93}Nb is largely bypassed. Indeed, normal AGB stars, while showing in their spectra the unstable ^{99}Tc, which is shorter-lived with respect to ^{93}Zr, are instead Nb-poor. On this basis one would find that AGB stars contribute minimally to the nuclei that immediately descend from ^{93}Nb itself, like the unstable ^{94}Nb and its decay daughter ^{94}Mo, whose s-process contribution was recently found to be of 1 to few percents (Stephan et al. 2019; Busso et al. 2021). However, due to the high abundance contrast (^{92}Zr and ^{94}Zr are more abundant than ^{94}Mo in the Sun by about a factor of 10), even a small leakage from the ^{93}Zr decay to

[6] https://www.nndc.bnl.gov/ensdf/

^{93}Nb (say, 1%) would contribute significantly to the chain ^{93}Nb–^{94}Nb–^{94}Mo. In summary, although ^{94}Mo remains a mainly-p nucleus, it cannot be excluded that it may receive a contribution from the s-process larger than estimated by Busso et al. (2021). On the other hand, the whole remaining abundance of ^{93}Zr decays to Nb at the end of the TP-AGB stage. Therefore, when the star is in a binary system exchanging mass between the components (i.e. is a so-called Ba-star), ^{93}Nb accumulates on the surface of the companion. When this last evolves to the AGB stage and undergoes *s*-processing in its turn, neutron captures will occur on a material that is Nb-enhanced, albeit by limited amounts (less than about 2-3 times the initial abundance) due to dilution in the envelope at the red giant stage. One of these very peculiar evolved stars, rich in both ^{99}Tc and ^{93}Nb, was recently observed by Shetye et al. (2020) and defined to be a *bi-intrinsic* AGB star. In such an object, a peculiar *s*-processing will occur, feeding more effectively ^{94}Mo. Although the effect is probably not large, due to the mentioned dilution, the *s*-process contribution to ^{94}Mo remains for the above reasons quite uncertain. This fact may affect the attempts at accounting for the Mo isotopic admixture of presolar SiC grains, where the ratio ^{94}Mo/^{96}Mo plays an important role. Experimental clarifications of the nuclear data (decay and cross sections) for this rather peculiar channel (^{93}Zr-^{93}Nb-^{94}Nb-^{94}Mo) would therefore be welcome.

A further source of uncertainty for the Zr isotopes concerns the β^-unstable ^{95}Zr. As mentioned, its (n,γ) cross section is still purely theoretical, although an experimental method to determine it (and the ones of other short-living *s*-process nuclei acting as branching points of the flow) was discussed by Sonnabend et al. (2004) using data of the inverse (γ,n) reactions. According to this discussion and to the one presented by Lugaro et al. (2003), improvements can be expected essentially only from new estimates of the cross section itself, as the decay rate seems to be well determined. In particular, the ground level (a $5/2^+$ state with a half-life of 64.02 days) decays to ^{95}Nb and then to ^{95}Mo with probably little to no dependence on the temperature conditions, because of the very high energy of the excited states.

3.4. *Mo*

The element Mo plays an important role for reconstructing the pollution of the solar system in *s*-process elements and its heterogeneity, as discussed by Stephan & Davis (2021). The same authors clarify how the trend of isotope ratios in presolar grains is separate from the meteoritic ones, very well defined and characteristic of *s*-processing environments in AGB stars. Here, the lightest Mo isotope that can receive some (marginal) contribution from *s*-processing in AGB stars is ^{94}Mo. Although we already mentioned that it is basically a *p*-process nucleus, in evolved low-mass stars it can be fed by neutron captures destroying ^{92}Mo, through the daughter of this last, ^{93}Mo. As it is shown by Figure 5, two channels then lead to ^{94}Mo from this source: a direct link via n-captures on ^{93}Mo itself (radioactive via e$^-$-captures, with a half-life of 4000y), or an indirect one, through the decay product ^{93}Nb, undergoing n-captures to ^{94}Nb. This last then can either decay to ^{94}Mo (β^--decay, with half-life of $2{\cdot}10^4$ yr) or participate to further neutron captures, feeding ^{95}Nb (half-life 35 days) and ^{96}Nb. In this respect, the channel from ^{94}Nb merges (on one side) with the already mentioned contribution coming from the initial ^{93}Nb abundance (and/or its refurbishing in the rare case of a bi-intrinsic AGB star). On the other side, it also starts new branching reactions on further unstable Nb isotopes. Concerning heavier Mo isotopes, we must notice that the solar system abundance of ^{96}Mo, which is an *s*-only nucleus, is reproduced very well by present *s*-process models (Liu et al.

2019; Busso et al. 2021). Improvements in nuclear data would therefore mainly help in clarifying details of the r and p processes, through their contributions to Mo isotopes, which are precisely predicted by presolar grain measurements (Stephan et al. 2019). The recommended cross sections of Mo isotopes from the K1 compilation almost coincide with the values listed in the *BNL* site (with exclusion of the unstable ^{99}Mo, where the *BNL* value, from the ENDF/B and JEFF collaborations, is higher: 481 against 366±92 mb: the effects of this alternative choice is again tested in our V2 cases). The uncertainty is in any case high, as only theoretical estimates are available. For other Mo isotopes, where experimental data exist, they are however quite old, so that new measurements are required and are actually already planned by the n_TOF collaboration (Guerrero et al. 2013). For that purpose, Liu et al. (2019) stressed the importance to have precise neutron capture cross sections as a function of the temperature even in energy regions not yet explored by activation techniques. On the other hand, a search for improvements in decay rates may concentrate on the subtle contribution to ^{94}Mo from ^{94}Nb mentioned above.

3.5. *Cs and Ba*

The s-process contribution to the element Ba starts from neutron captures on the stable isotope ^{133}Cs, whose recommended cross section is indicated to be 502±28 mb in K1, in agreement within the error bar with most of the values quoted at the *BNL* site. In nucleosynthesis models, the production of this nucleus is in its turn affected by the choice one makes for the initial abundance of Xe, whose average concentration in the solar system is unknown (Lodders 2021). When knowledge of tiny details is required, this implies some remaining ambiguity on the absolute levels of production for Ba isotopes.

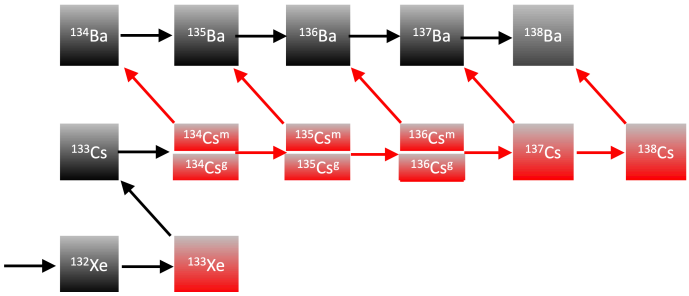

Figure 6. The s-process nucleosynthesis path trough Cs and Ba isotopes (thus in the region around $N = 82$). The ^{134}Cs and ^{135}Cs branching points are highlighted by red arrows. Same color code as in Figure 4.

As Figure 6 shows, after ^{133}Cs, the flux proceeds through a branching point at the radioactive ^{134}Cs, where n-captures compete mainly with β^- decay (laboratory half-life of 2 yr) to excited states of ^{134}Ba and, much less effectively, with electron captures to ^{134}Xe (half-life of $6.8{\cdot}10^5$ yr). From ^{134}Cs, neutron captures feed the longer-lived ^{135}Cs, whose half-life would require a specific reanalysis (see below), and then ^{136}Cs (half-life of 13.16 d) and ^{137}Cs (half-life of 30.07 y), which are sites of branching points for the s-process path, but whose decay rates remain essentially unchanged for varying temperatures.

This is not so for ^{134}Cs and ^{135}Cs. According to the computations (made under conditions of thermodynamic equilibrium) by Takahashi & Yokoi (1987), at $3{\cdot}10^8$K (a temperature rather typical of TPs) the decay rate of ^{134}Cs is enhanced with respect to the laboratory by a factor of about 200. However, these phenomenological computations are affected by large uncertainties that could be reduced with better nuclear parameters obtained through more modern approaches. As discussed in Busso et al. (2021), when one assumes the rate of ^{134}Cs de-

cay from Takahashi & Yokoi (1987), the galactic production of ^{134}Ba and ^{136}Ba (two *s*-only nuclei) does not fit the solar constraints very well. This point will be analyzed separately in next section, as an example of the general need for better weak interactions along the *s*-path. Also the half-life of ^{135}Cs might deserve a specific reanalysis and this would be so in particular if the decay rate of ^{134}Cs were to be reconsidered, with a larger production of ^{135}Cs itself (see the next two sections). Even following the Takahashi & Yokoi (1987) recommendations, in the temperature and density conditions prevailing in *TPs*, the half-life of ^{135}Cs would be of the order a few hundred years, thus inducing some branching effect in the *s*-process chain. In our computations, we consider the possibility of a reduced efficiency in the ^{134}Cs decay, hence of an increased importance of the ^{135}Cs branching, in our V2 cases.

Concerning the cross sections of Ba isotopes themselves, the K1 repository quotes for them rather small uncertainties (always less than 10%) and the Maxwellian-averaged data are either taken directly from recent measurements or renormalized according to Massimi et al. (2010); Lederer et al. (2011).

4. WEAK INTERACTION IMPROVEMENTS: THE CASE OF ^{134}CS

4.1. *Requirements from nucleosynthesis*

In the analysis of the nuclear parameters presented so far, we mainly concentrated on cross sections, but occasionally we met crucial decay processes whose accuracy one would like to see improved for clarifying important branching points. We consider here the example of the ^{134}Cs decay, affecting the isotopic admixture of Ba and the effectiveness of the branching point at ^{135}Cs. As mentioned, the two stable nuclei more heavily affected by the decay at ^{134}Cs are ^{134}Ba and ^{136}Ba, whose status as purely *s*-process nuclei is not reproduced very well by galactic neutron-capture nucleosynthesis, when the decay rate is taken from Takahashi & Yokoi (1987). See also, for this, Prantzos et al. (2018, 2020).

An illustration of this uncertain behavior is attempted in Figure 7. It shows the production factors from a model AGB star of 2 $M_\odot$, for a metallicity slightly lower than solar, which represents a sort of average model for galactic *s*-processing, in the sense that it naturally generates *s*-elements in solar proportions (see discussion of this point in Trippella et al. 2016; Busso et al. 2021). In particular, the figure shows purely *s*-nuclei in the atomic mass range from 125 to 150. They are displayed in logarithmic scale, normalized to the average production factor of *s*-nuclei, which is indicated on the plot. For the computations of the first panel (left) the nuclear parameters of the ST choice discussed above were adopted and it is clear that in such a case there is a discrepancy between ^{134}Ba and ^{136}Ba that is on average larger than for nearby *s*-nuclei. To level their production (right panel) one needs to assume that the temperature dependence of the decay rate for ^{134}Cs is less steep than suggested by Takahashi & Yokoi (1987) by a rather large factor (in the illustrative example shown, we changed it by a factor of 8). This confirms the finding by Cristallo et al. (2015), who obtained a 5% decrease of ^{134}Ba abundance by decreasing the ^{134}Cs decay by a factor of three. We notice that a similar leveling would have also been possible by changing upward the cross section of ^{134}Cs by more than a factor of two. Although the accepted value is from theoretical calculations, the possibility of such a large variation seems today unlikely.

4.2. *A revised β^- half life for ^{134}Cs*

Very recently a study by Simonucci et al. (2021, to be submitted) confirmed that the temperature dependence of the ^{134}Cs $\beta-$decay rate should indeed be less steep than so far assumed. In their approach, the Dirac-Hartree-

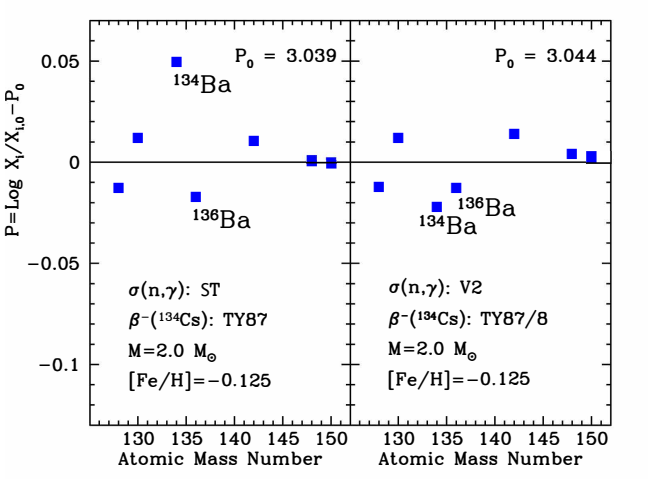

Figure 7. The distribution of normalized production factors of *s*-only nuclei in the atomic mass range 125 to 150. In the left panel, with our standard choice (ST) of nuclear parameters, ^{134}Ba and ^{136}Ba show some noticeable discrepancy. In the right panel, with the choice V2 for nuclear parameters, they are reconciled (the residual difference of their production factor with respect to unity is not significant, especially in the light of the absence of a secure datum for the solar concentration of the precursor Xe and of the uncertainties on the ^{133}Cs cross section). In order to obtain the result of the right panel the decay rate of ^{134}Cs to ^{134}Ba was assumed to have a temperature dependence less steep than suggested by Takahashi & Yokoi (1987) by a factor of 8.

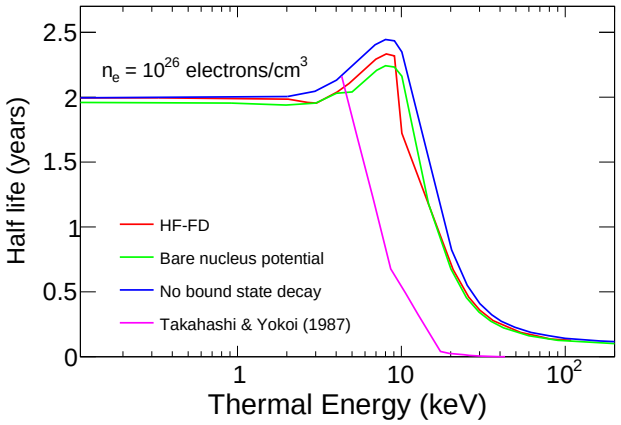

Figure 8. The half-life of ^{134}Cs as a function of the thermal energy (k_BT) estimated by using: (i) a Hartree-Fock (HF) mean-field potential with a Fermi-Dirac (FD) probability distribution (red line); (ii) same, but excluding the decay to bound states (blue line, no Fermi-Dirac temperature, orbitals are occupied in their HF ground state); (iii) Takahashi & Yokoi (1987, magenta line); (iv) the bare nucleus potential (green line).

Fock equations were solved for both the electron phase and the nucleus, modeling the nucleon-nucleon interaction through a relativistic one-body Wood-Saxon potential and factorizing the hadronic and leptonic currents as two non-interacting parts, also including the contributions from bound-state decays. Figure 8 shows that in the temperature range relevant for He-burning in the AGB stages, the new half-life, as obtained by the authors, is longer than in Takahashi & Yokoi (1987) by a factor ranging from 2.5 (near 8-10 keV) to more than 30 (at 30 keV). In particular, the red line includes the contribution to the half-life of ^{134}Cs of the atomic electrons, which populate the atomic orbitals according to a Fermi-Dirac distribution function (Morresi et al. 2018), while in the blue curve the electrons are clamped down to the electronic ground state (zero-temperature, close to laboratory conditions). In the latter case, the half-life is indeed higher as escaping β^- electrons are prevented by Pauli's exclusion principle from occupying bound orbitals (that are fully occupied) and can only be emitted in the continuum.

Here one is forced to wait for future measurements of the decay rate in ionized plasmas, hoping that these calculations and the previously-mentioned astrophysical suggestions can find in that way an experimental confirmation.

4.3. *Foreseen experimental revisions*

For the scope mentioned in the previous subsection we analyzed in some detail the real possibility that a variation in the rate of the β^- decay of ^{134}Cs and of other radionuclei by factors similar to the one inferred by the new calculations there shown can be measured in ionized plasma environments.

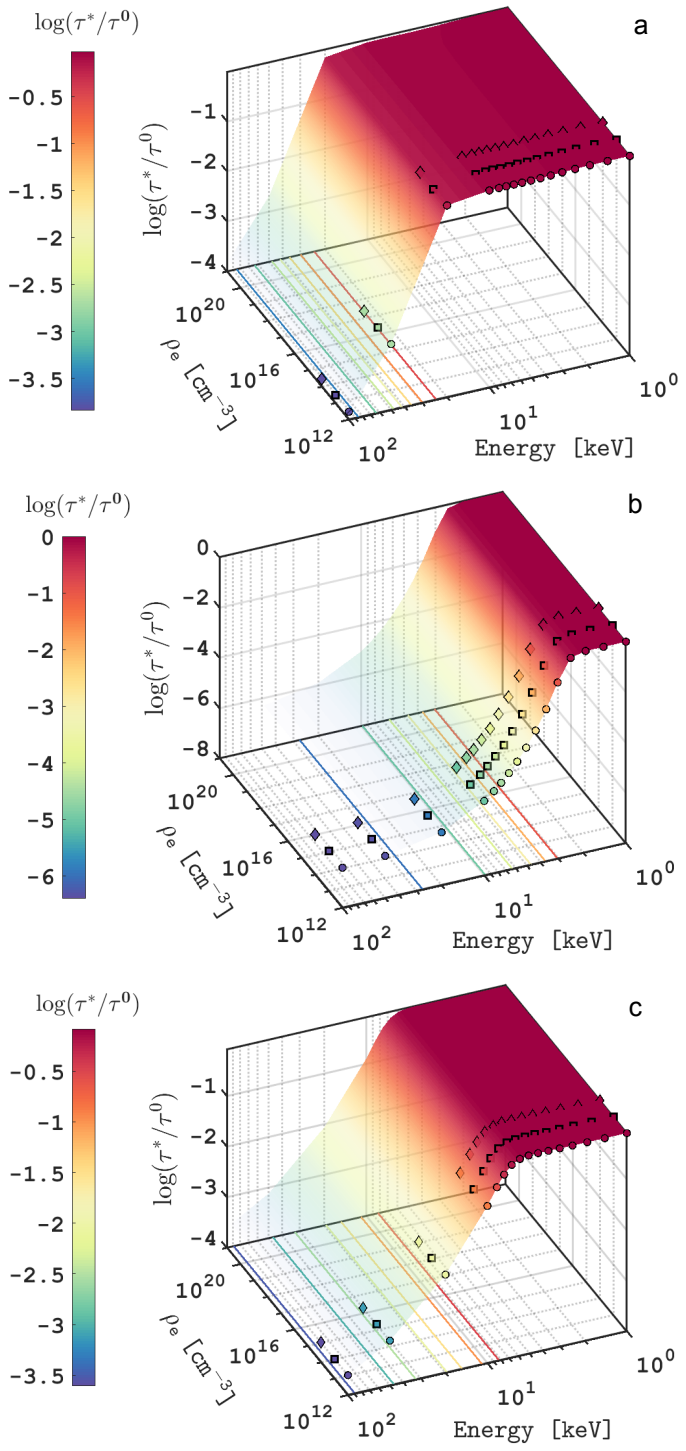

Figure 9. Mean lifetime in ionized plasma as a function of the plasma density (in the range $\rho_e \sim 10^{12} - 10^{21}$ cm^{-3}) and of the energy (in the range $k_B T_e \sim 1 - 10^2$ keV) for β^- decays of (**a**) $^{93}_{40}$Zr→$^{93}_{41}$Nb, (**b**) $^{94}_{41}$Nb→$^{94}_{42}$Mo, and (**c**) $^{134}_{55}$Cs→$^{134}_{56}$Ba. The color bar (log-scale) indicates the ratio τ^*/τ^0. Terrestrial average lifetimes τ^0 are (**a**) $2.32 \cdot 10^6$ yr, (**b**) $2.93 \cdot 10^4$ yr, and (**c**) 2.98 yr. Marker-points are shown only for densities accessible by the PANDORA plasmas.

In this framework, the PANDORA project (Plasmas for Astrophysics, Nuclear Decay Observation and Radiation for Archaeometry, Mascali et al. 2017, 2020) aims to measure for the first time β-decay rates in controlled ionized plasmas made of radionuclides, at different plasma densities and temperatures. The innovative PANDORA plasma trap (presently under construction at LNS-INFN) will be able to produce and confine plasmas with electron-ion densities up to 10^{13} cm^{-3} and electron temperatures T_e in the range $0.1 - 30$ keV. These conditions would mimic some important aspects of stellar environments, in particular the charge states. More in detail, the experimental approach consists in determining a direct correlation of the plasma properties with the nuclear decay itself. This will be achieved by simultaneously identifying and discriminating, via a multi-diagnostic system, the γ-ray products following β-decays from unstable isotopes and the photons self-emitted by the plasma (Naselli et al. 2019, 2020). PANDORA has been designed in order to maintain the radionuclides in a dynamical equilibrium for several days or even weeks. Indeed, simulations of the γ-decay detection efficiency (as a function of the radionuclide lifetime and of the effective activity in the plasma volume) show that the minimum measurement time needed to achieve a sufficiently accurate measure ($\geq 3\sigma$) ranges from hours to several days, depending on the isotope under investigation.

Virtual experiments have been performed to study the feasibility of measuring the decay rates of several nuclei in the PANDORA trap and to predict possible enhancements of weak-interaction rates in stellar environments. Among the cases of study there are several nuclei involved in s-process nucleosynthesis, ^{93}Zr, ^{94}Nb and ^{134}Cs in particular. The charge state distribution (CSD) in the plasma of these isotopes was investigated, starting from a "stellar-

like" scenario and down to the PANDORA density range, by using the FLYCHK population kinetics code (Chung et al. 2005). This was done in both local thermodynamic equilibrium (LTE) and non-LTE conditions. FLYCHK can estimate the probability for each ion stage to be populated, together with the mean charge state of the plasma species, according to the atomic-level population distribution and the plasma thermodynamics. Once the radionuclide CDSs have been modeled in non-LTE conditions, the in-plasma $\beta-$decay rates of ^{93}Zr, ^{94}Nb and ^{134}Cs can be estimated. This is illustrated in Figure 9, which shows the behavior of the $\log(\tau^*/\tau^0)$ (namely the log-ratio between the lifetime in stellar conditions and the one in terrestrial conditions τ^0) for the nuclei studied, as a function of the plasma density ρ_e and of the thermal energy k_BT_e. Calculations show that the plasma temperature affects largely the isotope decay rates and that temperature effects dominate over those related to density. This finding strengthens the credibility of the half-lives in stellar conditions that will be estimated from experimental data taken by PANDORA in its operating density range. The results of this analysis will be discussed in detail for a larger sample of radionuclides in a forthcoming paper.

5. PRESOLAR SIC-GRAIN MEASUREMENTS.

5.1. *General remarks*

In general, the observed properties of the stars becoming C-rich during their AGB evolution match well those expected in the range 1 to 3 $M_\odot$(Abia et al. 2020), where the lowest masses pertain to older objects, dynamically distributed similarly to the old disk population (Claussen et al. 1987). There is also a tail for more massive members (up to maybe 4 or 5 $M_\odot$), which can be identified with very red objects, belonging to the thin disk, as early noticed by Barnbaum et al. (1991). In this rather wide range, the AGB stars that are the main parents of presolar grains have been recently suggested to be about 2 $M_\odot$, with metallicities close to the solar one (Cristallo et al. 2020). This suggestion, especially for what concerns the metallicity, is in accordance with the ages of presolar SiC grains recovered from the Murchison chondrite, which have been estimated by Heck et al. (2020), based on the cosmogenic ^{21}Ne produced inside those solids, from ^{21}Na decay. Most (60%) of the grains turned out to be older than the solar system by less than 300 Myr, with a minority showing ages up to 3 Gyr. According to recent estimates of the relations between age and abundances for various representative elements in the galactic disk (Nissen et al. 2020; Feuillet et al. 2019; Sharma et al. 2020) we expect a rather small spread of metallicities across the above mentioned age span at the galactic radius of the solar system. For these reasons, and in agreement with Cristallo et al. (2020), our comparisons between model predictions and observed isotopic ratios in SiC grains will be restricted to a small spread, $-0.15 \lesssim [Fe/H] \lesssim 0.1$. In those comparisons, the mentioned suggestions lead us to expect that stellar models of about 2 $M_\odot$ explain most of the SiC grain constraints.

5.2. *The Main-Stream SiC Grains and their Age*

SiC crystals form the most abundant sample of presolar grains and are among the most precise tools available to constrain *s*-process nucleosynthesis and the ensuing envelope enrichment in AGB stars. Some dust particles of AGB origin were captured in pristine meteorites, showing us the isotopic composition of the stellar winds where they were formed. The laboratory measurements of the isotopic admixtures for trace heavy elements in such SiC grains offer then diagnostic tools for the composition of evolved red giants that cannot be obtained from their stellar spectroscopy, which is ham-

pered on one hand by variability of the stellar sources and on the other by restriction to elemental abundances in most cases.

Among the families of presolar SiC grains so far recovered, the largest one (more than 16500 grains, according to Stephan et al. 2020) is that of *Main-Stream* (hereafter MS) grains. Their isotopic ratios of C, N and Si, along with traces of s-elements measured in a subset of them, certify their AGB origins (Zinner 2014). So far, Sr, Zr, Mo or Ba isotopic ratios have been measured only in 214 MS-SiC grains out of the several thousands available in the database maintained at the Washington University in St. Louis (Hynes & Gyngard 2009). For none of the grains the isotopic ratios were measured for all the 4 elements. However, in most cases data about the isotopic mix of Ba and at least of one or two of the other elements are available. Many authors determined the isotopic composition for smaller subsets of the 214 grains using different techniques, e.g. Resonance Ionization Mass Spectrometry (RIMS) or Nano-Secondary Ion Mass Spectrometry (NanoSIMS).

The results are reported in several papers (Nicolussi et al. 1997, 1998; Jennings et al. 2002; Savina et al. 2003; Barzyk et al. 2007; Marhas et al. 2007; Liu et al. 2014, 2015, 2018; Stephan et al. 2018, 2019). Despite this fragmented scenario, data from the different samples show common trends for the measured values of the isotopic ratios, as shown in Figure 10. There (as well as in any reference to isotopic ratios presented in this work) the data are shown in the so-called δ notation, where, for example:

$$\delta\left(\frac{^{135}\mathrm{Ba}}{^{136}\mathrm{Ba}}\right) = 10^3 \cdot \left[\left(\frac{^{135}\mathrm{Ba}}{^{136}\mathrm{Ba}}\right) / \left(\frac{^{135}\mathrm{Ba}}{^{136}\mathrm{Ba}}\right)_{\odot} - 1\right]$$

The mentioned concordant collective behaviors are maintained despite the different techniques adopted and the different research groups involved, thus revealing a remarkable strength in the constraints posed by MS-SiC data to *s*-process nucleosynthesis. In addition to the MS samples, the cited authors determined the isotope ratios for Sr, Zr, Mo and Ba also in a few tens of further presolar SiC grains, which have been classified as U (unknown), due to lack of clear data about C or N isotopic ratios. Since the heavy element isotopic ratios shown by grains of the U group are in agreement with the ones from the MS-SiC family, it is reasonable to believe that they are of AGB origins, too. We shall therefore use both the grain samples for the comparison with nucleosynthesis predictions of our models. For an easier reading, in the figures showing the comparisons we represent the SiC isotopic ratio data with grey dots, independently of the authors who actually did the measurements. The only distinction we maintain is the one between the MS and U families, which are plotted by filled and empty dots, respectively.

6. COMPARING MODELS AND MEASUREMENTS: A FEW RESULTS

6.1. *Sr versus Ba isotopic ratios*

We start the comparisons of model predictions with measurements in presolar SiC grains by considering the relative behavior of the isotopes of two crucial elements (Sr and Ba), characterizing the neutron flow at the neutron magic numbers $N = 50$ and $N = 82$.

Figure 11 illustrates the case of the measured isotopic ratios $^{88}\mathrm{Sr}/^{86}\mathrm{Sr}$ and $^{135}\mathrm{Ba}/^{136}\mathrm{Ba}$, as compared to predictions from our 2 $\mathrm{M}_{\odot}$ models and reveals some interesting details. In general, the area covered by the measurements and the one covered by the models overlap largely (see especially the panel at the right side). This indicates that the quality of the nuclear parameters, as adopted after the discussion of section 3, is already rather satisfactory. However, important improvements are possible. Let us analyze this situation in some detail. As shown by the left panel of Figure 11, models for the C-rich phases in the envelopes tend to produce inter-

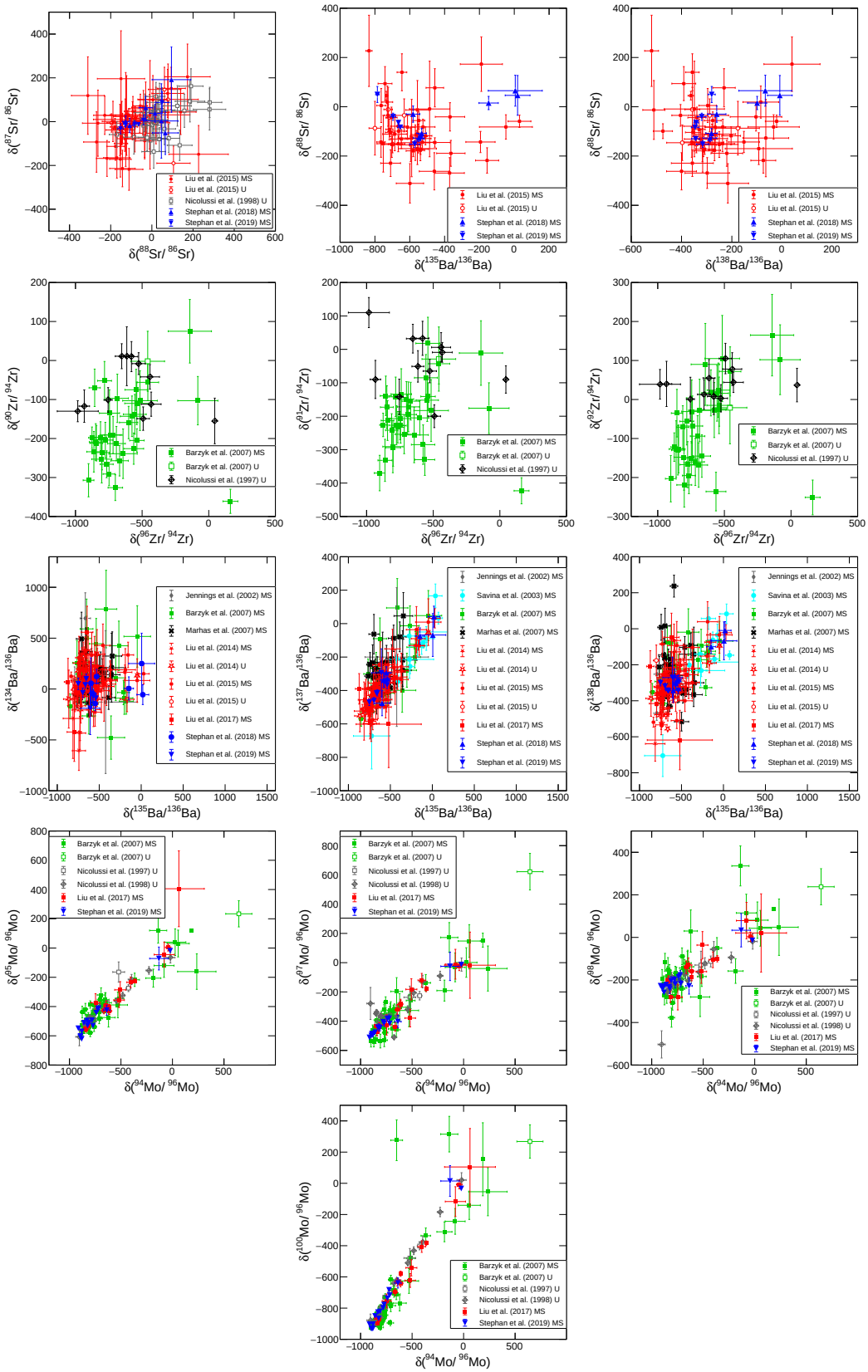

Figure 10. The whole sample of MS and U presolar SiC grains, for which the database of the Washington University in St. Louis reports values for the Sr, Zr, Mo and/or Ba isotopic ratios (Hynes & Gyngard 2009; Stephan et al. 2020, and references therein). Grain data were measured by several authors, as indicated by the legends. See text for details.

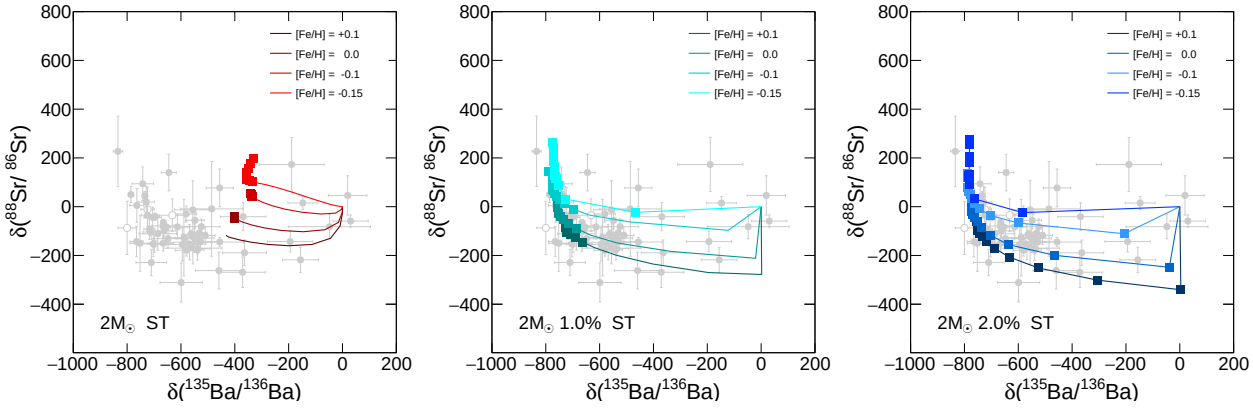

Figure 11. A comparison of nucleosynthesis predictions from $2M_\odot$ models (full lines) with SiC measurements (represented by gray dots with error bars, in the delta notation defined in the text). The case of the isotopic ratios $^{88}Sr/^{86}Sr$ and $^{135}Ba/^{136}Ba$ is shown. The first panel (left) shows the envelope composition. There, full squared dots represent model abundance ratios achieved after TDU episodes that follow *TP*s, provided the envelope has reached a composition with C/O > 0.8 (see Busso et al. 2021). The central panel shows the isotopic ratios in the magnetized winds, as defined in section 2.2, if the percentage of He-shell material introduced in them by breaking magnetic flux tubes it at the level of 1%. The last panel (right) represents the same situation as the central one, but for a percentage of He-shell material of 2%. Also in these other two panels full squares indicate the *TPs* were the wind has a C/O ratio larger than 0.8.

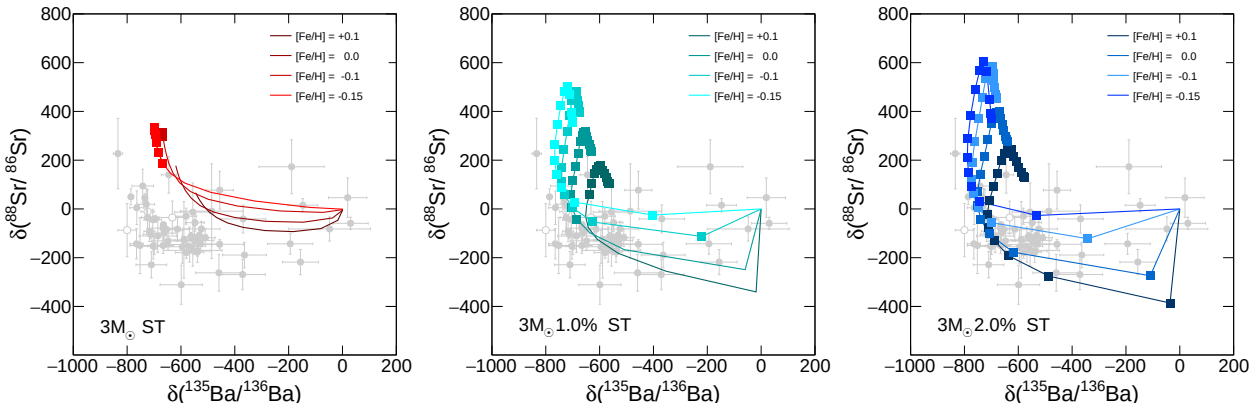

Figure 12. Same as Figure 11, but for models of 3 $M_\odot$ stars.

mediate delta values for the ratio $^{135}Ba/^{136}Ba$, not suited to cover the wide area of the measurements. This problem was common in previous approaches in the literature (see e.g. Lugaro et al. 2018). When instead we consider the magnetized winds discussed in the text (see section 2.2), their compositions sample a wider distribution of $^{135}Ba/^{136}Ba$ ratios, and cover increasing portions of the measurement area for increasing amounts of the He-shell material added in them. They can actually account for these SiC data almost completely, as shown in the right panel of Figure 11. This fact shows the relevance of this wind component, not considered so far in the literature. Anyhow, further improvements in the model predictions might be welcome if one wants to refer also to 3 $M_\odot$ models. Their behavior with respect to the experimental constraints is illustrated in Figure 12 for the same cases chosen in the previous plot. As is clear, with our standard choice of the nuclear parameters these models should be excluded. Indeed, when they cover the whole range of $^{135}Ba/^{136}Ba$ data (see full lines with heavy dots

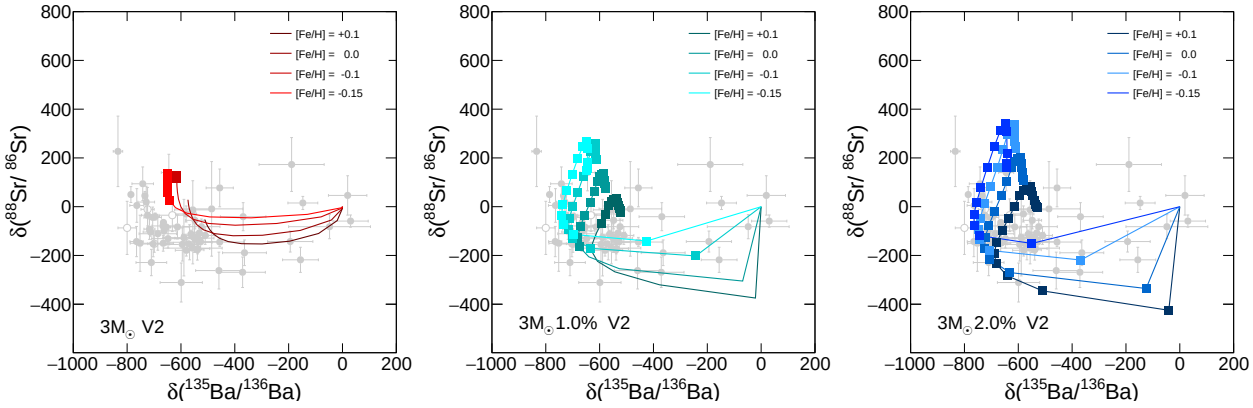

Figure 13. Same as Figure 12, but for the test models V2, with tentatively modified nuclear inputs (see section 3).

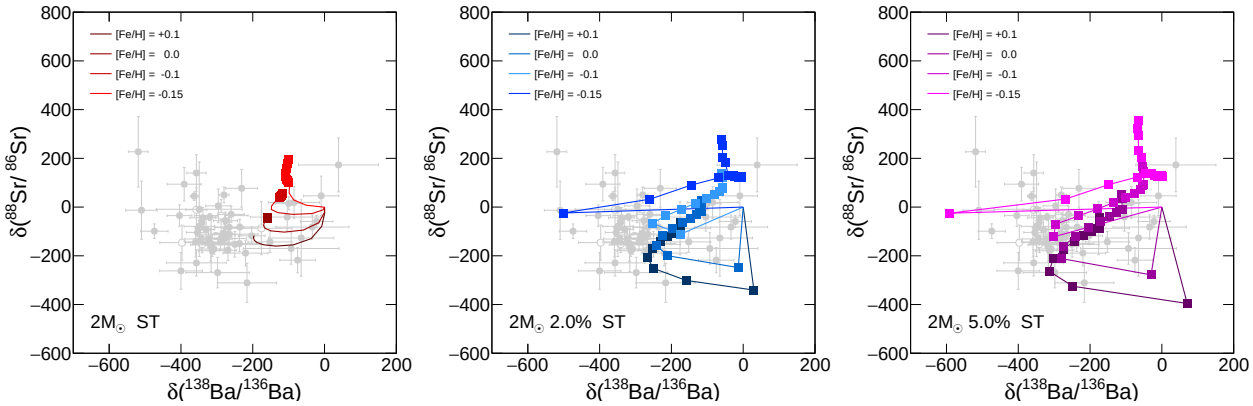

Figure 14. A comparison of model predictions with SiC data (with notations as defined in Figure 11) for the isotopic ratios $^{88}Sr/^{86}Sr$ and $^{138}Ba/^{136}Ba$. The first panel (left) shows the envelope composition, the central panel shows the isotopic ratios in the magnetized winds when the percentage of He-shell material in them is 2%. The panel at the right side refers again to the winds, but for a percentage of He-shell material of 5%

.

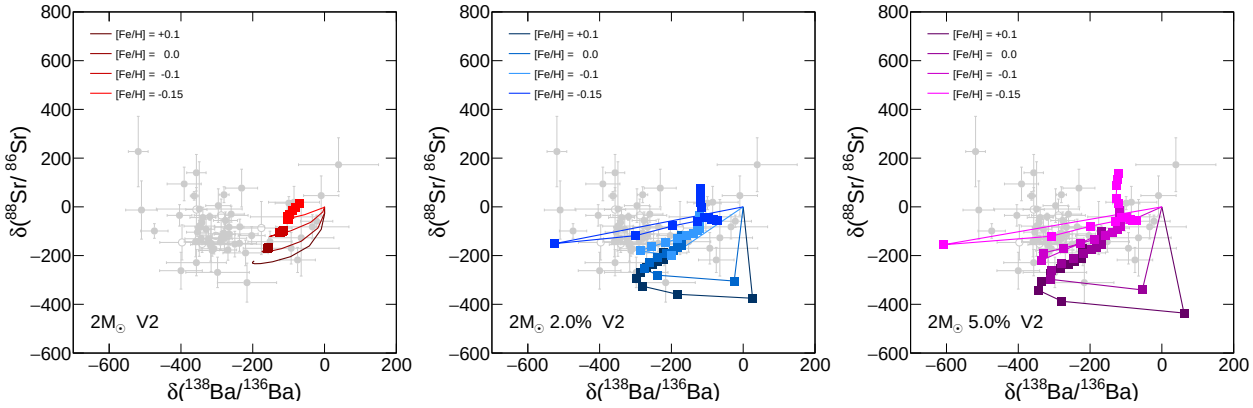

Figure 15. A plot similar to Figure 14, but for test models V2, with tentatively modified nuclear input parameters (see section 3).

in Figure 12), their Sr isotopic ratio in the ordinate extends at too high δ-values, where there

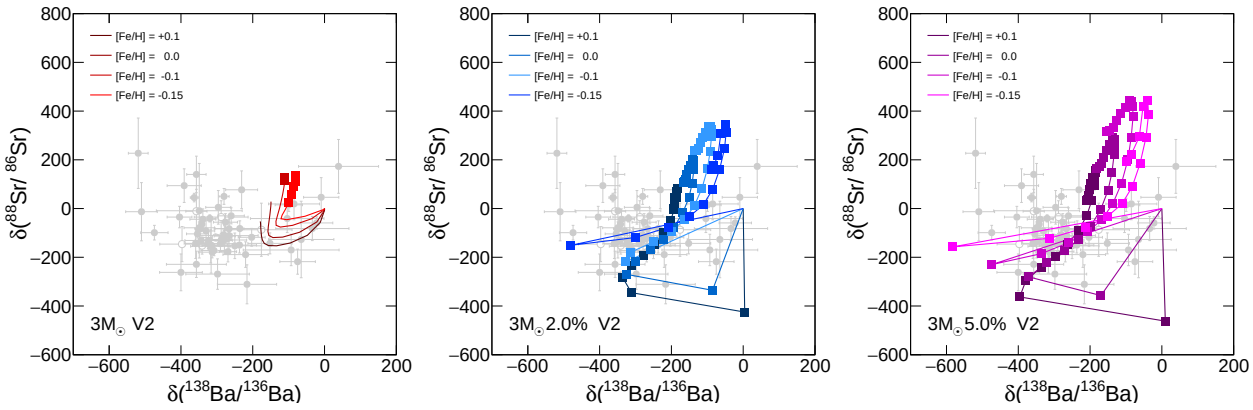

Figure 16. A plot similar to Figure 15, but for 3 $M_\odot$ models.

are no measurements. This is due to the higher efficiency, in these more massive models (due to the higher pulse temperature) of the reaction branch that from ^{85}Kr feeds ^{86}Kr, ^{87}Rb and ^{88}Sr (see section 3.1). Can we exclude completely, on this basis, that SiC grains be formed, at least in part, by stars more massive than 2 $M_\odot$ at the adopted metallicities? The previous analysis by Lugaro et al. (2018), on the basis of the same troubles with the Sr versus Ba plot, concluded in this way and suggested to move to higher-than-solar metallicities (where the reduced neutron exposure feeds ^{88}Sr less efficiently). We don't really know if this is a solution, but we think that such a conclusion might be too drastic, in the light of our previous discussion of Sr cross sections (see section 3.2). Indeed, with our test choice V2 of the parameters (where, for the cross section of ^{88}Sr, we adopted the value measured by Katabuchi et al. 2011, larger by 30% with respect to the K1 recommendations) the situation changes considerably, as shown in Figure 13. As is illustrated there, in this case the range of predictions from 3 $M_\odot$ models for the ^{88}Sr/^{86}Sr ratio shrinks sharply. The right panel of Figure 13 would represent now a quite good reproduction of experimental data, without invoking excessively high metallicities, which we consider unlikely for presolar grains (in this case the fits of Figure 11 would not be modified largely). We leave for the moment this possible indication as a warning on the ^{88}Sr neutron-capture cross section.

We can also notice that the ^{135}Ba/^{136}Ba ratios (and in general those for Ba isotopes of higher atomic mass) are sensitive to further uncertain nuclear parameters, namely the (n,γ) cross sections for the radioactive Cs isotopes ^{134}Cs and ^{135}Cs, for which only theoretical values exist, and their β^- decay rates. In addition to the already discussed case of ^{134}Cs, indeed (see section 4), also the case of ^{135}Cs is worth a dedicated study, as its dependence on temperature is large above $2{\cdot}10^8$ K and might well be different than assumed here from Takahashi & Yokoi (1987). A slightly longer half-life (so far estimated to be of the order of a few hundred years in *TP* conditions) would modify the ratio ^{135}Ba/^{136}Ba in a complex way, with the effect of further stretching the area of the measurements covered by envelope and wind models with respect to what is obtained in Figures from 11 to 13. Similar effects would be induced by variations in the ^{135}Cs neutron-capture cross section.

Another crucial test for nucleosynthesis models and their nuclear parameters emerges from the δ-values of ^{88}Sr/^{86}Sr, when plotted as a function of the ones for ^{138}Ba/^{136}Ba. Figure 14 shows the situation for a 2 $M_\odot$ star: here we illustrate the composition of the envelope and that of magnetized winds (with 2% to 5% of He-shell material admixed). Even in this 2 $M_\odot$ case, in our estimates a considerable fraction of the

TPs (full dots) would produce in the winds values of $^{88}Sr/^{86}Sr$ that are higher than measured (see in particular the right panel). This fact may, again, play in favor of a larger ^{88}Sr neutron capture cross section than recommended in the K1 database, as illustrated in Figure 15, where the shrinking in the dispersion of the ordinate is obtained by adopting the already mentioned choice V2 for the nuclear parameters.

Even more evident in Figures 14 and 15 is that there is some excess of ^{138}Ba in the models. This nucleus is at the $N = 82$ magic number and is fed effectively when the neutrons available are abundant. However, this is not the case in the computations shown here, which refer to solar-like metallicities (hence to stars with high contents of Fe), with rather small neutron exposures. A solution, especially for the 2 $M_\odot$ case, would be to accept that magnetized winds be generated with even larger fractions of He-shell matter than displayed in the figures, as the model curves perform a U-turn that reaches down to lower and lower values of the $^{138}Ba/^{136}Ba$ ratio for increasing mixing fractions. This solution, however, would be restricted to the 2 $M_\odot$ models, as those for the 3 $M_\odot$ cases with high mixing ratios tend to produce values excessively positive in the Sr isotopic ratio in the ordinate, even in the test case V2. This is indeed illustrated in Figure 16. The best compromises for the 3 $M_\odot$ cases seem to be limited to 1-2% of mixing of He-shell matter in the winds. Alternatives exist, but must invoke further changes in the nuclear parameters. As mentioned, these might affect the decay rates of ^{135}Cs and the cross sections of radioactive Cs isotopes.

On the other hand, the nuclear data on barium neutron capture cross sections are satisfactorily precise at large enough temperatures (T$\sim$ 300 MK), but are rather loosely constrained at lower energies (around 8 keV, i.e. the energy characterizing neutron release in the ^{13}C pocket). Also in this case, refinements in the experimental data are urgently needed.

6.2. *Sr and Ba isotopes separately*

A comparison of model predictions with the measured δ-values for Sr isotopes is shown in Figures 17 and 18, adopting for illustration a 2 and a 3 $M_\odot$ model, respectively. We refer directly to the cases V2, discussed in the previous section, because the excess production of ^{88}Sr there identified can be avoided. As is made clear in the Figure 18, in a 3 $M_\odot$star the envelope alone (left panel) does not offer a good reproduction of the measurements, while referring to the magnetized winds allows for a much better agreement, which improves when the percentage of He-shell material in the outflows increases (central and right panels).

The cases for 2 $M_\odot$ stellar models (Figure 17) look similar, but with a lower proportion of the area containing experimental data covered by models. It can be noticed that the large spread in the measured data for ^{87}Sr is not well matched by model curves. Actually, such a spread can best be interpreted as a consequence of a range of temperature values (i.e. of stellar masses), in which the complex path leading to ^{87}Sr varies. In this respect, the unique value for the branching ratio at ^{84}Kr to the isomer of ^{85}Kr, which we are forced to assume from the K1 repository, in the absence of different data, is certainly an oversimplified assumption (see section 3.1). Here we clearly need new nuclear physics measurements on the chains departing from Kr isotopes, in this case the one proceeding through $^{85}Kr^m$, ^{85}Rb, ^{86}Rb and $^{86,87}Sr$. In general, therefore, the evidence provided so far by SiC grains points to the needs of revisions in the nuclear parameters discussed in sections 3.1 and 3.2.

Concerning the various Ba isotopes, Figures 19 and 20 illustrate a synthesis of what can be obtained for them in representative cases among those discussed so far. In particular, we

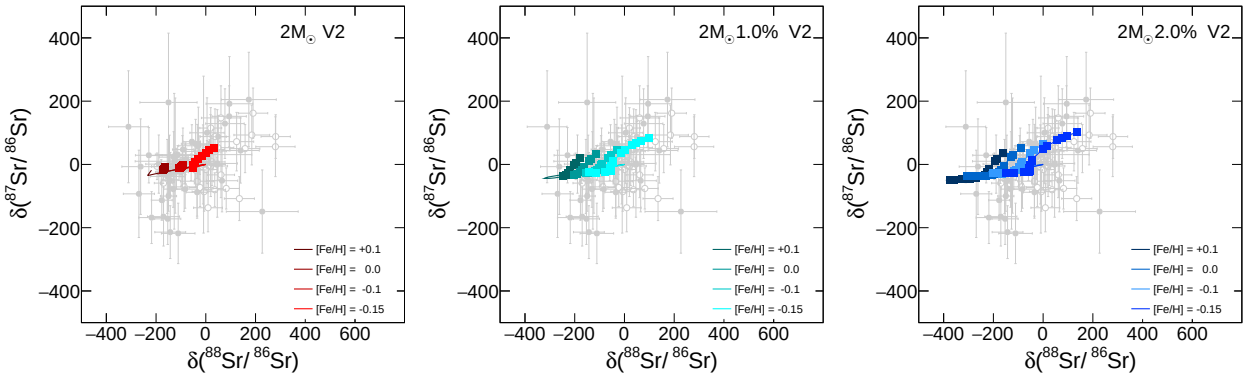

Figure 17. A comparison of model predictions from 2 $M_\odot$ models of various metalliciities (full lines with heavy dots) with SiC data for Sr isotopes. The meaning of the symbols is the same as in previous figures, and the three panels represent again the envelope (left) and magnetized winds with 2% (central) and with 5% (right) of He-shell material added.

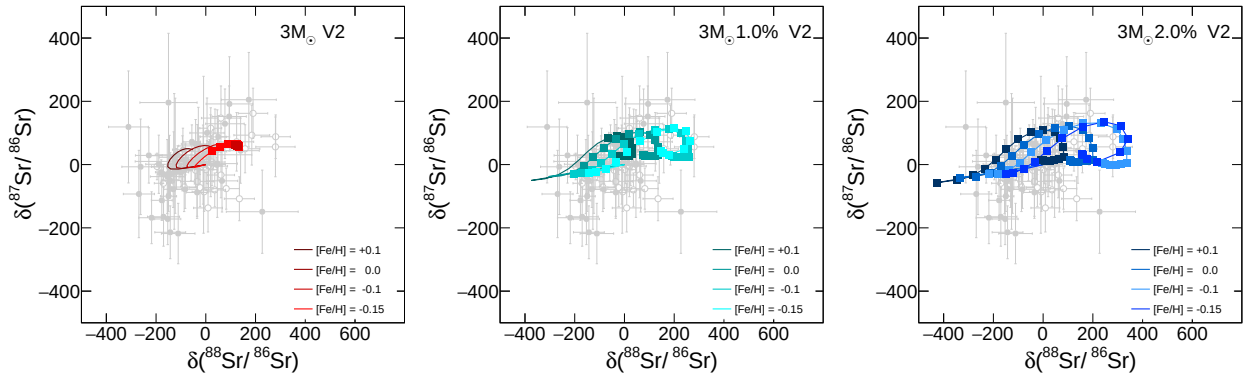

Figure 18. Same plots of Figure 17, but for 3 $M_\odot$ models.

plot there situations pertaining to magnetized winds, with 5% admixture of material from the He-shell for 2 $M_\odot$ models and 2% for 3 $M_\odot$ ones. This latter case seems to represent a rough average condition permitting to reproduce sufficiently well the three-isotope plots of barium, including the constraints from ^{134}Ba, ^{137}Ba and ^{138}Ba. Despite the good accord, these plots confirm that small revisions in the decay rates or in the cross sections for Cs isotopes, leading to wider spreads in ^{137}Ba and ^{138}Ba, would be welcome.

6.3. *Isotopic ratios for Zr and Mo*

The isotopic ratios involving Zr, as measured in SiC grains, appear to pose much smaller problems to AGB models and the nuclear parameters seem to be in this case sufficiently good. This is so also for isotopes that were so far quoted by other groups as being problematic, like ^{92}Zr (Lugaro et al. 2014) and which are instead compatible with our magnetized winds. Also for the Zr ratios, therefore, including this wind component largely increases the mutual compatibility of data and models, improving considerably over previously published analyses. We show here, in Figure 21 and in Figure 22 a couple of synthetic, representative cases, involving ^{90}Zr/^{94}Zr, ^{92}Zr/^{94}Zr, and ^{96}Zr/^{94}Zr.

Figure 21 presents the data for the ^{90}Zr/^{94}Zr ratio as a function of ^{96}Zr/^{94}Zr, compared to the outputs from a choice of our models for the winds. Panels at the left and at the center re-

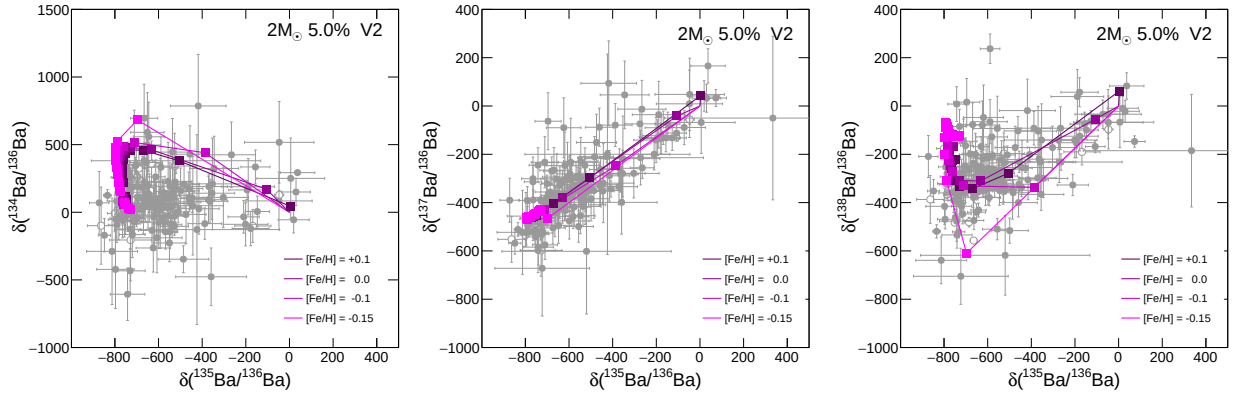

Figure 19. A comparison of model predictions from a representative case of 2 $M_\odot$ models (full lines with heavy dots) with SiC data for various Ba isotopes and with the the choice V2 for nuclear parameters, including revisions for the ^{134}Cs decay, as illustrated in section 4. The meaning of the symbols is the same as in previous figures. The three panels represent the composition of winds with 5% of He-shell material added.

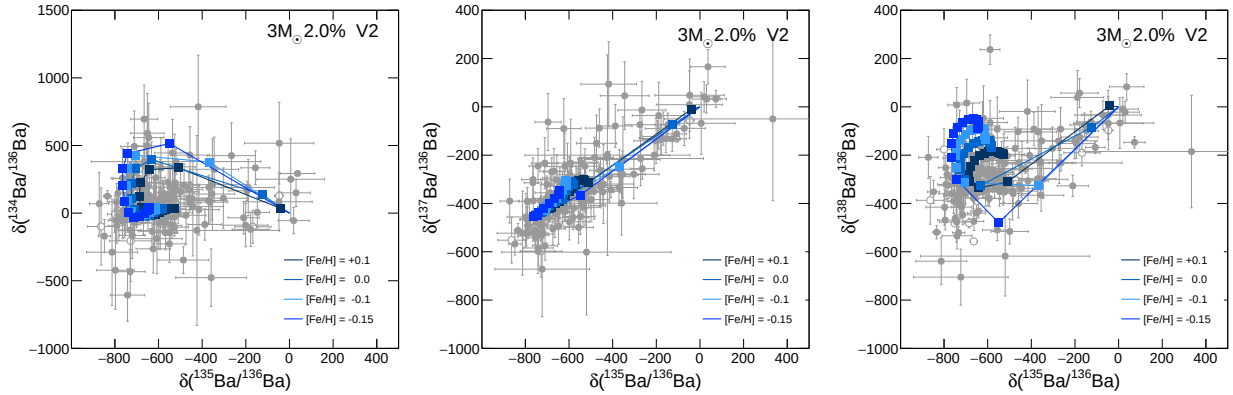

Figure 20. A plot similar to Figure 19, but for 3 $M_\odot$ models and a dilution of He-shell material in the wind of 2%.

fer to 2 $M_\odot$ models with 1% and 2% admixtures of He-shell materials, respectively, while the right panel represents the case of 3 $M_\odot$ models at 0.5% dilution. The three plots together show how the measurements can be well accounted for by the ensemble of our models, with 2 $M_\odot$ cases explaining better the vertical spread and 3 $M_\odot$ ones complementing them for the horizontal distribution. No special change in the nuclear parameters seems necessary.

Figure 22 then illustrates the situation with ^{92}Zr. Previous attempts in the literature (Lugaro et al. 2014) concluded that δ-values of ^{92}Zr in excess of -50 could not be explained by AGB models. Here, instead, we see that 2 $M_\odot$ models are sufficient to account for the data, provided we considered various He-shell admixtures. Grains with higher δ values for ^{92}Zr/^{94}Zr are explained by progressively higher percentages of mixing. In the plots provided we consider the composition of the winds for increasing He-shell admixtures, where grains with progressively higher δ values for ^{92}Zr/^{94}Zr are found. In this respect we recall the present complex picture of AGB winds illustrated by Höfner & Olofsson (2018), as enhanced mass loss rates and dust production in phases preceding the final superwinds are probably needed to support our model. Flaring activity might actually lead to

such enhanced mass loss rates and dust formation (Soker & Kastner 2003).

Concerning Mo, Stephan et al. (2019) showed how its isotopic mix seems to derive from a combination of essentially only two components, one purely s-process controlled, the second of isotopically solar composition. In this condition, as is known, the data in three-isotope plots distribute along almost straight diagonal lines. Beyond this simple trend, however, there are tiny details, from which new lessons can be learned.

Models for the C-rich envelopes tend to represent rather exstreme admixtures, very close to the *s*-process end-member (see the discussion in Liu et al. 2019) The composition of the magnetized winds, instead, allows us to cover larger and larger portions of the area filled by the data, for increasing efficiencies of He-shell matter mixed. This is so because in the winds, through the mechanism sketched in Figure 3, one samples small portions of the C-rich component transported by magnetized structures and large portions of the envelope, even in phases preceding the final ones of the C-star formation. As mentioned, small but important details reveal, even here, that something needs to be improved. Let us review these details, starting with inspection of Figures from 23 to 26, all representing the envelop composition (left panels) and winds of 2 $M_\odot$ models, enriched at the 0.5% and the 2% in C-rich material (central and right panels, respectivelly). We choose the ratio ^{94}Mo/^{96}Mo as a common abscissa and the first evidence is that the models at the TDU episodes (full dots) crowd at δ values for ^{94}Mo which are slightly, but clearly, too low with respect to the measured data. Some increase in ^{94}Mo would solve the problem and we believe that this is an indication either of a smaller value of its neutron-capture cross section than recommended in the K1 repository, or of the need to invoke for ^{94}Mo the subtle contributions from the chain passing through ^{93}Nb and ^{94}Nb. Another evidence is shown by the heaviest isotopes ^{97}Mo, ^{98}Mo and ^{100}Mo, see Figures from 26 to 28; the last two comparing the data with 3 $M_\odot$ models, the previous one with 2 $M_\odot$ models. Here, the straight diagonal line represents an average trend, over which some significant vertical spread exist, at different levels for the different isotopes. This behavior is not accounted for with our standard choice of the nuclear parameters, but can instead be interpreted by referring to our test case V2. Among the changes there introduced (see section 6.3), we enhanced the cross section of ^{95}Zr to its upper limit allowed by the K1 recommendations, to take into account the suggestions for a larger cross section contained in the *BNL* repository. We also adopted, for ^{99}Mo, the larger value provided by the same *BNL* site. Figures 27 and 28 show the effects of these changes on the plots involving ^{98}Mo and ^{100}Mo, in our 3 $M_\odot$ models. In particular, Figure 27 shows the effects, on ^{98}Mo, of the first of the mentioned changes. Increasing the (n,γ) cross section of ^{95}Zr has the effect of feeding more efficiently the chain ^{96}Zr, ^{97}Zr, ^{97}Nb, ^{97}Mo, at the expense of ^{96}Mo. As a consequence, this last is slightly reduced. Since it is at the denominator of the isotopic ratio in the ordinate, its decrease induces higher values of the latter. Indeed, as the figure shows, in 3 $M_\odot$ models one has originally a downward spread (left panel) in the model trend, worsening the fit with respect to the 2 $M_\odot$ cases, while with the V2 choice the direction of the spread is reverted. Should one correct slightly ^{94}Mo in the way already discussed, this would result in fitting quite well even the small dispersion of the observed points. A very similar change is induced by the test case V2 on ^{100}Mo, this time being the direct effect of the larger cross section adopted for ^{99}Mo, as illustrated in Figure 28.

We also recall that, in the case in which the abundance of a nuclide in grains is extremely

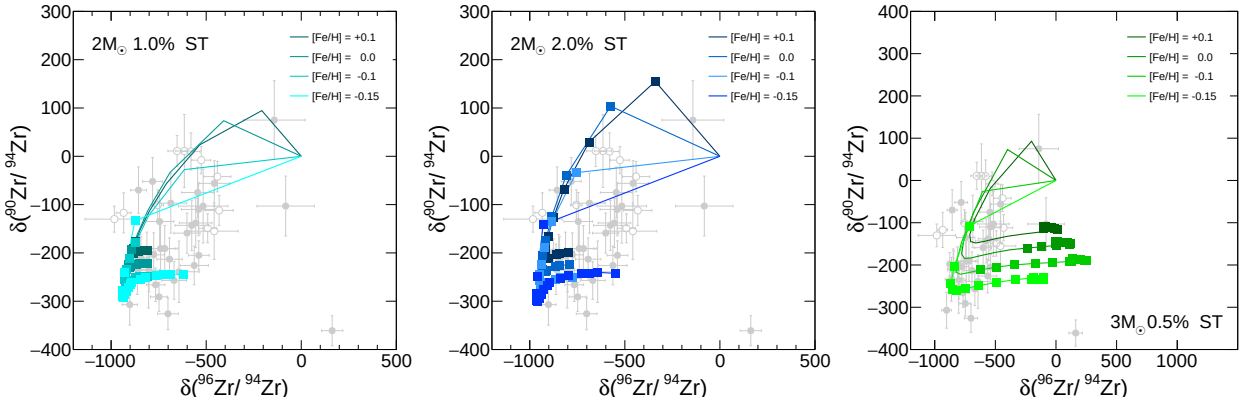

Figure 21. The comparison of measured SiC data involving ^{90}Zr with model sequences for the winds of 2 $M_\odot$ stars at 1% and 2% dilution of He-shell matter in the winds (left and center panels) and for those of 3 $M_\odot$ stars with a low percentage (0.5%) of He-shell matter added (right panel).

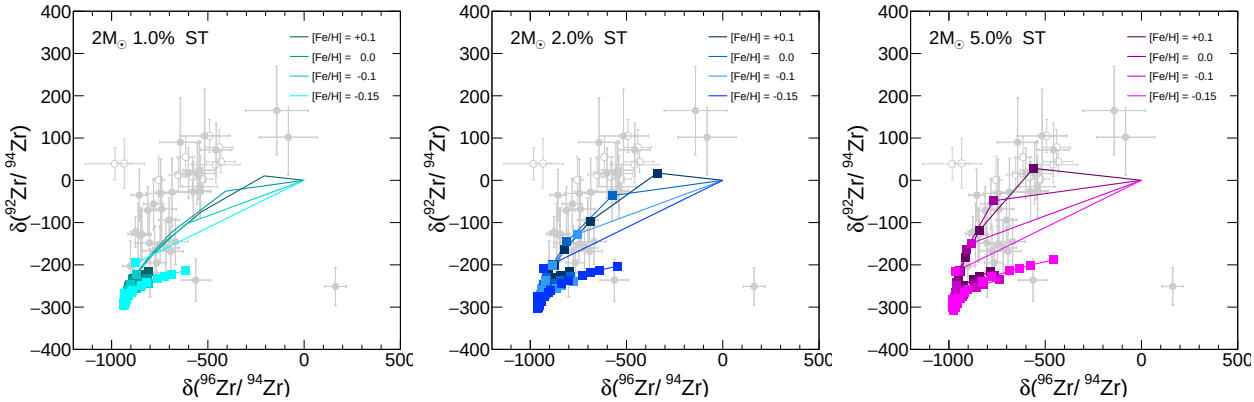

Figure 22. The comparison of measured SiC data involving ^{92}Zr with model sequences for the winds of 2 $M_\odot$ models, for progressively higher (from left to right) amounts of He-shell matter added.

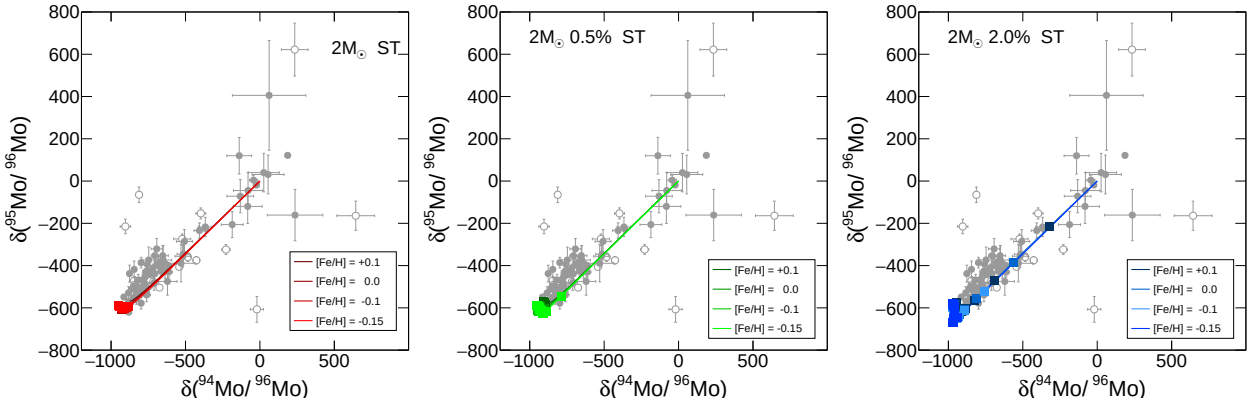

Figure 23. The measured SiC δ values for ^{95}Mo/^{96}Mo and ^{94}Mo/^{96}Mo as compared to model sequences for the envelope (left) and for two mixing cases (center and right) in the magnetized winds of 2 $M_\odot$ stars.

poor, thus making very small also a connected isotopic ratio, a minimum sample pollution (for example if a grain is coated by a very thin residue of solar matter) could affect the measured value in such a way to mimic a dilution of the progenitor stellar winds with further unpol-

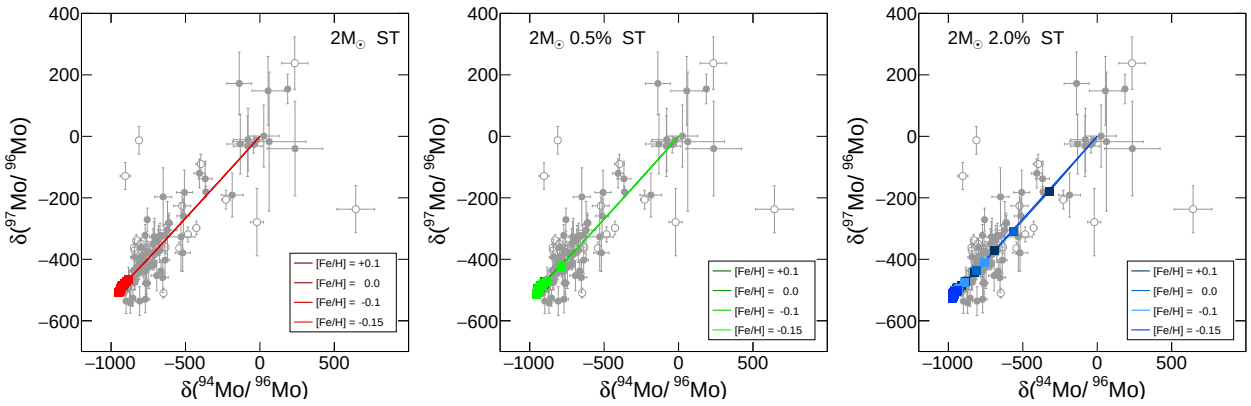

Figure 24. Same as Figure 23, but with the ratio ^{97}Mo/^{96}Mo in the ordinate.

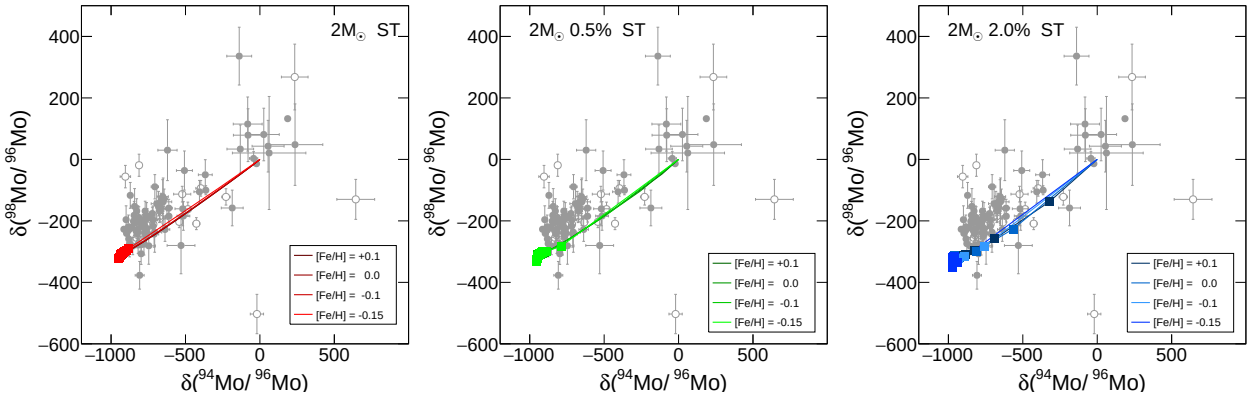

Figure 25. Same as Figure 23, but with the ratio ^{98}Mo/^{96}Mo in the ordinate.

luted solar material (Lugaro et al. 2017). This fact may account for the composition of grains that show Mo isotopic admixtures close to the solar values.

7. CONCLUSIONS

In this paper we analyzed the isotopic composition of heavy neutron capture elements measured in presolar MS-SiC grains of AGB origins, interpreting them as the outcome of *s*-process nucleosynthesis occurring in the AGB stages of stars in the mass range 2−3 $M_\odot$, with close to solar metallicities (with [Fe/H] values from −0.15 to +0.1). In the reference models we adopted the scheme of magnetically-induced mixing discussed in previous paper from our group and the composition of the stellar winds were simulated taking into account the effects of flares and/or mass ejection from magnetic structures ascending from the He-intershell and breaking in the outer layers of the atmosphere, depositing there C-rich matter and *s*-processed heavy elements.

The comparisons made use of nuclear parameters available in the present literature, in particular adopting most neutron capture cross sections from the Kadonis 1.0 compilation (K1) and weak interaction rates from Takahashi & Yokoi (1987).

We found that our specific mixing scheme, discussed here in detail for the first time, greatly enhances the general agreement between model predictions and observed isotopic ratios (expressed in the δ notation) and on this basis we suggest that magnetic fields in AGB stars are important not only for driving neutron capture processes, but also for mixing their products into the circumstellar envelopes.

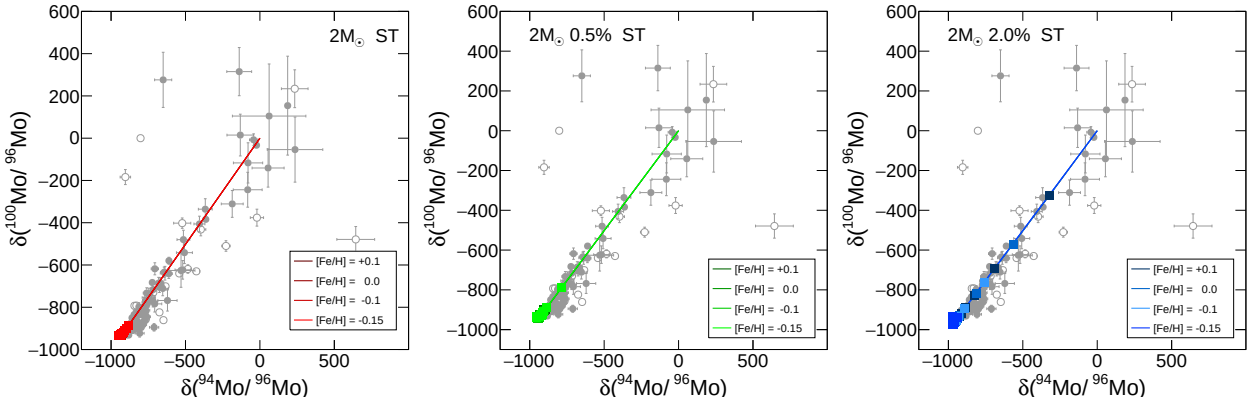

Figure 26. Same as Figure 23, but with the ratio ^{100}Mo/^{96}Mo in the ordinate.

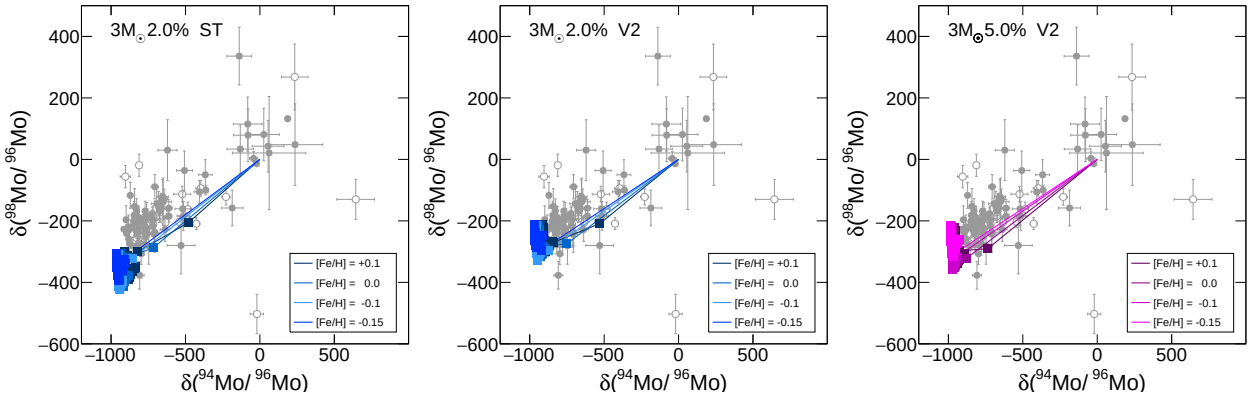

Figure 27. Same as Figure 25, but for a 3 $M_\odot$ star, in which the left panel shows the standard wind case, for a dilution of 2%, while the center and right panels show the V2 case, for dilutions of 2% and 5%, respectively.

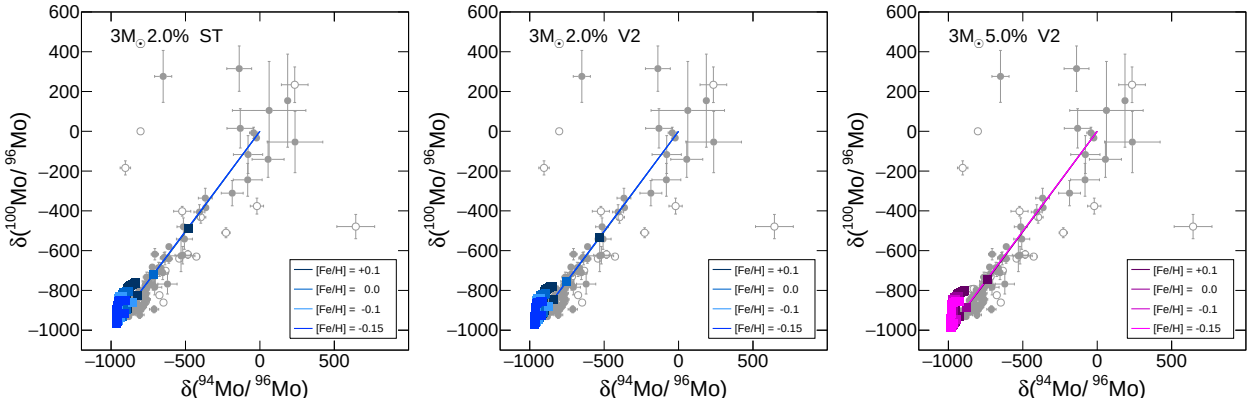

Figure 28. Same as Figure 26, but for a 3 $M_\odot$ star, in which the left panel shows the standard wind case, for a dilution of 2%, while the center and right panels show the V2 case, for dilutions of 2% and 5%, respectively.

When the details of the comparisons (involving isotopic ratios of *s*-process elements near the $N = 50$ and $N = 82$ neutron magic numbers) are concerned, an analysis of the input nuclear parameters and of their uncertainties leads us to identify a series of crucial points on which new

measurements would be welcome, both for the neutron capture cross sections and for the decay rates of radionuclei in stellar plasmas. On this last point, we presented an anticipation from a work to be submitted, in which we showed how more precise theoretical studies of crucial decays can lead to remarkable changes in the rates commonly used in stellar models, available through the Takahashi & Yokoi (1987) work. We showed in particular how, in the example case of ^{134}Cs, the temperature enhancement of its rate is less steep than so far assumed by important factors (from 2.5 to about 30). On the basis of simulations of the operation of the plasma trap PANDORA (now under construction), we also suggested that variations of the type found in our theoretical approach should be easily verified experimentally in the next few years.

Using test computations with ad-hoc modified input nuclear parameters, we also indicated where future nuclear physics efforts should concentrate. This includes re-evaluations of the branching ratios on ^{84,85}Kr and of neutron captures for ^{88}Sr, ^{95}Zr, the Mo and Ba isotopes and the unstable nuclei ^{134,135}Cs. We also suggested that measurements of the weak interaction rates of ^{94}Nb and ^{135}Cs in ionized plasmas should immediately follow those of ^{134}Cs.

On the basis of the results possible with slightly modified values of the crucial input parameters, which are presently in the range permitted by uncertainties, we find that there is no need to invoke stars considerably more metal-rich than the Sun as sources for presolar grains, as sometimes suggested in the literature.

ACKNOWLEDGMENTS

The PANDORA collaboration acknowledges the support of the Third Committee of the Italian Institute for Nuclear Physics (INFN-CSN3). DV acknowledges the financial support from the German-Israeli Foundation (GIF No. $I-1500-303.7/2019$)

REFERENCES

Abia, C., Cristallo, S., Cunha, K., de Laverny, P., & Smith, V. V. 2019, A&A, 625, A40, doi: 10.1051/0004-6361/201935286

Abia, C., Cunha, K., Cristallo, S., & de Laverny, P. 2015, A&A, 581, A88, doi: 10.1051/0004-6361/201526586

Abia, C., de Laverny, P., Cristallo, S., Kordopatis, G., & Straniero, O. 2020, A&A, 633, A135, doi: 10.1051/0004-6361/201936831

Abia, C., Domínguez, I., Gallino, R., et al. 2003, PASA, 20, 314, doi: 10.1071/AS03021

Adsley, P., Battino, U., Best, A., et al. 2021, PhRvC, 103, 015805, doi: 10.1103/PhysRevC.103.015805

Arlandini, C., Käppeler, F., Wisshak, K., et al. 1999, ApJ, 525, 886, doi: 10.1086/307938

Ayres, T. R., Linsky, J. L., Vaiana, G. S., Golub, L., & Rosner, R. 1981, ApJ, 250, 293, doi: 10.1086/159374

Aznar Cuadrado, R., Jordan, S., Napiwotzki, R., et al. 2004, A&A, 423, 1081, doi: 10.1051/0004-6361:20040355

Bagnulo, S., & Landstreet, J. D. 2020, A&A, 643, A134, doi: 10.1051/0004-6361/202038565

Bahcall, J. N. 1962, ApJ, 136, 445, doi: 10.1086/147398

Barnbaum, C., Kastner, J. H., & Zuckerman, B. 1991, AJ, 102, 289, doi: 10.1086/115876

Barzyk, J. G., Savina, M. R., Davis, A. M., et al. 2007, Meteoritics and Planetary Science, 42, 1103, doi: 10.1111/j.1945-5100.2007.tb00563.x

Bauer, R. W., Bazan, G., Becker, J. A., Howe, R. E., & Mathews, G. J. 1991, PhRvC, 43, 2004, doi: 10.1103/PhysRevC.43.2004

Bisterzo, S., Gallino, R., Straniero, O., Cristallo, S., & Käppeler, F. 2012, MNRAS, 422, 849, doi: 10.1111/j.1365-2966.2012.20670.x

Bisterzo, S., Gallino, R., Käppeler, F., et al. 2015, MNRAS, 449, 506, doi: 10.1093/mnras/stv271

Busso, M., Gallino, R., Lambert, D. L., Travaglio, C., & Smith, V. V. 2001, ApJ, 557, 802, doi: 10.1086/322258

Busso, M., Gallino, R., & Wasserburg, G. J. 1999, ARA&A, 37, 239, doi: 10.1146/annurev.astro.37.1.239
Busso, M., Palmerini, S., Maiorca, E., et al. 2010, ApJL, 717, L47, doi: 10.1088/2041-8205/717/1/L47
Busso, M., Vescovi, D., Palmerini, S., Cristallo, S., & Antonuccio-Delogu, V. 2021, ApJ, 908, 55, doi: 10.3847/1538-4357/abca8e
Busso, M., Wasserburg, G. J., Nollett, K. M., & Calandra, A. 2007, ApJ, 671, 802, doi: 10.1086/522616
Chadwick, M. B., Herman, M., Obložinský, P., et al. 2011, Nuclear Data Sheets, 112, 2887, doi: 10.1016/j.nds.2011.11.002
Charbonnel, C., & Lagarde, N. 2010, A&A, 522, A10, doi: 10.1051/0004-6361/201014432
Chung, H.-K., Chen, M., Morgan, W., Ralchenko, Y., & Lee, R. 2005, High Energy Density Physics, 1, 3, doi: https://doi.org/10.1016/j.hedp.2005.07.001
Claussen, M. J., Kleinmann, S. G., Joyce, R. R., & Jura, M. 1987, ApJS, 65, 385, doi: 10.1086/191229
Cristallo, S., Abia, C., Straniero, O., & Piersanti, L. 2015, ApJ, 801, 53, doi: 10.1088/0004-637X/801/1/53
Cristallo, S., Nanni, A., Cescutti, G., et al. 2020, A&A, 644, A8, doi: 10.1051/0004-6361/202039492
Cristallo, S., Straniero, O., Gallino, R., et al. 2009a, ApJ, 696, 797, doi: 10.1088/0004-637X/696/1/797
—. 2009b, ApJ, 696, 797, doi: 10.1088/0004-637X/696/1/797
Cristallo, S., La Cognata, M., Massimi, C., et al. 2018, ApJ, 859, 105, doi: 10.3847/1538-4357/aac177
Denissenkov, P. A., & Tout, C. A. 2003, MNRAS, 340, 722, doi: 10.1046/j.1365-8711.2003.06284.x
Denissenkov, P. A., & VandenBerg, D. A. 2003, ApJ, 593, 509, doi: 10.1086/376410
Dillmann, I., Heil, M., Käppeler, F., et al. 2006, in American Institute of Physics Conference Series, Vol. 819, Capture Gamma-Ray Spectroscopy and Related Topics, ed. A. Woehr & A. Aprahamian, 123–127, doi: 10.1063/1.2187846
Dillmann, I., Szücs, T., Plag, R., et al. 2014, Nuclear Data Sheets, 120, 171, doi: 10.1016/j.nds.2014.07.038
Duthu, A., Herpin, F., Wiesemeyer, H., et al. 2017, A&A, 604, A12, doi: 10.1051/0004-6361/201730485
Eggleton, P. P., Dearborn, D. S. P., & Lattanzio, J. C. 2006, Science, 314, 1580, doi: 10.1126/science.1133065
—. 2008, ApJ, 677, 581, doi: 10.1086/529024
Feuillet, D. K., Frankel, N., Lind, K., et al. 2019, MNRAS, 489, 1742, doi: 10.1093/mnras/stz2221
Gilroy, K. K., & Brown, J. A. 1991, ApJ, 371, 578, doi: 10.1086/169922
Goriely, S., Hilaire, S., & Koning, A. J. 2008, A&A, 487
Guerrero, C., Tsinganis, A., Berthoumieux, E., et al. 2013, The European Physical Journal A, 27, doi: 10.1140/epja/i2013-13027-6
Haisch, B., Schmitt, J. H. M. M., & Rosso, C. 1991, ApJL, 383, L15, doi: 10.1086/186230
Harris, M. J., Lambert, D. L., & Smith, V. V. 1985, ApJ, 299, 375, doi: 10.1086/163707
Heck, P. R., Greer, J., Kööp, L., et al. 2020, Proceedings of the National Academy of Science, 117, 1884, doi: 10.1073/pnas.1904573117
Herpin, F., Baudry, A., Thum, C., Morris, D., & Wiesemeyer, H. 2006, A&A, 450, 667, doi: 10.1051/0004-6361:20054255
Herpin, F., Chapman, J. M., Menten, K., et al. 2007, First 3mm molecular line survey of O-rich evolved objects, ATNF Proposal
Herwig, F. 2005, ARA&A, 43, 435, doi: 10.1146/annurev.astro.43.072103.150600
Herwig, F., Langer, N., & Lugaro, M. 2003, ApJ, 593, 1056, doi: 10.1086/376726
Höfner, S., & Olofsson, H. 2018, A&A Rv, 26, 1, doi: 10.1007/s00159-017-0106-5
Holzwarth, V., & Schüssler, M. 2001, A&A, 377, 251, doi: 10.1051/0004-6361:20011097
Hynes, K. M., & Gyngard, F. 2009, in Lunar and Planetary Science Conference, Lunar and Planetary Science Conference, 1198
Jennings, C. L., Savina, M. R., Messenger, S., et al. 2002, in Lunar and Planetary Science Conference, Lunar and Planetary Science Conference, 1833

Jordan, S., Werner, K., & O'Toole, S. J. 2005, in Astronomical Society of the Pacific Conference Series, Vol. 334, 14th European Workshop on White Dwarfs, ed. D. Koester & S. Moehler, 257. https://arxiv.org/abs/astro-ph/0410509

Kaeppeler, F., Gallino, R., Busso, M., Picchio, G., & Raiteri, C. M. 1990a, ApJ, 354, 630, doi: 10.1086/168720

Kaeppeler, F., Zhao, W. R., Beer, H., & Ratzel, U. 1990b, ApJ, 355, 348, doi: 10.1086/168769

Käppeler, F., Gallino, R., Bisterzo, S., & Aoki, W. 2011, Reviews of Modern Physics, 83, 157, doi: 10.1103/RevModPhys.83.157

Karakas, A. I., & Lattanzio, J. C. 2014, PASA, 31, e030, doi: 10.1017/pasa.2014.21

Katabuchi, T., Hai, N. C., Igashira, M., et al. 2011, Journal of Korean Physical Society, 59, 1844, doi: 10.3938/jkps.59.1844

Kawka, A., & Vennes, S. 2014, MNRAS, 439, L90, doi: 10.1093/mnrasl/slu004

Kemball, A. J., & Diamond, P. J. 1997, ApJL, 481, L111, doi: 10.1086/310664

Koehler, P. E., Winters, R. R., Guber, K. H., et al. 2000, PhRvC, 62, 055803, doi: 10.1103/PhysRevC.62.055803

Langer, N., Heger, A., Wellstein, S., & Herwig, F. 1999, A&A, 346, L37. https://arxiv.org/abs/astro-ph/9904257

Lederer, C., Colonna, N., Domingo-Pardo, C., et al. 2011, PhRvC, 83, 034608, doi: 10.1103/PhysRevC.83.034608

Linsky, J. L., & Haisch, B. M. 1979, ApJL, 229, L27, doi: 10.1086/182924

Liu, N., Gallino, R., Bisterzo, S., et al. 2014, ApJ, 788, 163, doi: 10.1088/0004-637X/788/2/163

Liu, N., Gallino, R., Cristallo, S., et al. 2018, ApJ, 865, 112, doi: 10.3847/1538-4357/aad9f3

Liu, N., Savina, M. R., Gallino, R., et al. 2015, ApJ, 803, 12, doi: 10.1088/0004-637X/803/1/12

Liu, N., Stephan, T., Cristallo, S., et al. 2019, ApJ, 881, 28, doi: 10.3847/1538-4357/ab2d27

Lodders, K. 2021, SSRv, 217, 44, doi: 10.1007/s11214-021-00825-8

Lugaro, M., Davis, A. M., Gallino, R., et al. 2003, ApJ, 593, 486, doi: 10.1086/376442

Lugaro, M., Karakas, A. I., Pető, M., & Plachy, E. 2018, GeoCoA, 221, 6, doi: 10.1016/j.gca.2017.06.006

Lugaro, M., Tagliente, G., Karakas, A. I., et al. 2014, ApJ, 780, 95, doi: 10.1088/0004-637X/780/1/95

Lugaro, M., Karakas, A. I., Bruno, C. G., et al. 2017, Nature Astronomy, 1, 0027, doi: 10.1038/s41550-016-0027

Magrini, L., Vescovi, D., Casali, G., et al. 2021, A&A, 646, L2, doi: 10.1051/0004-6361/202040115

Maiorca, E., Magrini, L., Busso, M., et al. 2012, ApJ, 747, 53, doi: 10.1088/0004-637X/747/1/53

Maiorca, E., Randich, S., Busso, M., Magrini, L., & Palmerini, S. 2011, ApJ, 736, 120, doi: 10.1088/0004-637X/736/2/120

Marhas, K. K., Hoppe, P., & Ott, U. 2007, Meteoritics and Planetary Science, 42, 1077, doi: 10.1111/j.1945-5100.2007.tb00562.x

Mascali, D., Musumarra, A., Leone, F., et al. 2017, European Physical Journal A, 53, 145, doi: 10.1140/epja/i2017-12335-1

Mascali, D., Busso, M., Mengoni, A., et al. 2020, in European Physical Journal Web of Conferences, Vol. 227, European Physical Journal Web of Conferences, 01013, doi: 10.1051/epjconf/202022701013

Massimi, C., Domingo-Pardo, C., Vannini, G., et al. 2010, PhRvC, 81, 044616, doi: 10.1103/PhysRevC.81.044616

Morresi, T., Taioli, S., & Simonucci, S. 2018, Advanced Theory and Simulations, 1, 1800086, doi: https://doi.org/10.1002/adts.201800086

Naselli, E., Mascali, D., Biri, S., et al. 2019, Journal of Instrumentation, 14, C10008, doi: 10.1088/1748-0221/14/10/C10008

Naselli, E., Mascali, D., Caliri, C., et al. 2020, in European Physical Journal Web of Conferences, Vol. 227, European Physical Journal Web of Conferences, 02006, doi: 10.1051/epjconf/202022702006

Nicolussi, G. K., Davis, A. M., Pellin, M. J., et al. 1997, Science, 277, 1281, doi: 10.1126/science.277.5330.1281

Nicolussi, G. K., Pellin, M. J., Lewis, R. S., et al. 1998, PhRvL, 81, 3583, doi: 10.1103/PhysRevLett.81.3583

Nissen, P. E., Christensen-Dalsgaard, J., Mosumgaard, J. R., et al. 2020, A&A, 640, A81, doi: 10.1051/0004-6361/202038300

Nordhaus, J., Busso, M., Wasserburg, G. J., Blackman, E. G., & Palmerini, S. 2008, ApJL, 684, L29, doi: 10.1086/591963
Nucci, M. C., & Busso, M. 2014, ApJ, 787, 141, doi: 10.1088/0004-637X/787/2/141
Palmerini, S., Trippella, O., Busso, M., et al. 2018, GeoCoA, 221, 21, doi: 10.1016/j.gca.2017.05.030
Pascoli, G. 2020, PASP, 132, 034203, doi: 10.1088/1538-3873/ab54a2
Pascoli, G., & Lahoche, L. 2008, PASP, 120, 1267, doi: 10.1086/594377
—. 2010, PASP, 122, 1334, doi: 10.1086/657508
Prantzos, N., Abia, C., Cristallo, S., Limongi, M., & Chieffi, A. 2020, MNRAS, 491, 1832, doi: 10.1093/mnras/stz3154
Prantzos, N., Abia, C., Limongi, M., Chieffi, A., & Cristallo, S. 2018, MNRAS, 476, 3432, doi: 10.1093/mnras/sty316
Pritychenko, B., & Mughabghab, S. F. 2012, Nuclear Data Sheets, 113, 3120, doi: 10.1016/j.nds.2012.11.007
Rauscher, T. 2012, ApJL, 755, L10, doi: 10.1088/2041-8205/755/1/L10
Roriz, M. P., Lugaro, M., Pereira, C. B., et al. 2020, MNRAS, doi: 10.1093/mnras/staa3888
Rosner, R., An, C. H., Musielak, Z. E., Moore, R. L., & Suess, S. T. 1991, ApJL, 372, L91, doi: 10.1086/186031
Rosner, R., Musielak, Z. E., Cattaneo, F., Moore, R. L., & Suess, S. T. 1995, ApJL, 442, L25, doi: 10.1086/187807
Sabin, L., Hull, C. L. H., Plambeck, R. L., et al. 2015a, MNRAS, 449, 2368, doi: 10.1093/mnras/stv461
Sabin, L., Wade, G. A., & Lèbre, A. 2015b, MNRAS, 446, 1988, doi: 10.1093/mnras/stu2227
Savina, M. R., Pellin, M. J., Tripa, C. E., et al. 2003, GeoCoA, 67, 3215, doi: 10.1016/S0016-7037(03)00082-6
Seeger, P. A., Fowler, W. A., & Clayton, D. D. 1965, ApJS, 11, 121, doi: 10.1086/190111
Sharma, S., Hayden, M. R., Bland-Hawthorn, J., et al. 2020, arXiv e-prints, arXiv:2011.13818. https://arxiv.org/abs/2011.13818
Shetye, S., Van Eck, S., Goriely, S., et al. 2020, A&A, 635, L6, doi: 10.1051/0004-6361/202037481
Shibata, K., Iwamoto, O., Nakagawa, T., et al. 2011, Journal of Korean Physical Society, 59, 1046, doi: 10.3938/jkps.59.1046
Soker, N., & Kastner, J. H. 2003, ApJ, 592, 498, doi: 10.1086/375686
Sonnabend, K., Mengoni, A., Mohr, P., et al. 2004, in American Institute of Physics Conference Series, Vol. 704, Tours Symposium on Nuclear Physics V, ed. M. Arnould, M. Lewitowicz, G. Münzenberg, H. Akimune, M. Ohta, H. Utsunomiya, T. Wada, & T. Yamagata, 463–472, doi: 10.1063/1.1737142
Soppera, N., Bossant, M., Dupont, E., Henriksson, H., & Rugama, Y. 2011, Journal of Korean Physical Society, 59, 1329, doi: 10.3938/jkps.59.1329
Stephan, T., & Davis, A. M. 2021, ApJ, 909, 8, doi: 10.3847/1538-4357/abd725
Stephan, T., Trappitsch, R., Hoppe, P., et al. 2019, ApJ, 877, 101, doi: 10.3847/1538-4357/ab1c60
Stephan, T., Trappitsch, R., Davis, A. M., et al. 2018, GeoCoA, 221, 109, doi: 10.1016/j.gca.2017.05.001
Stephan, T., Bose, M., Boujibar, A., et al. 2020, in Lunar and Planetary Science Conference, Lunar and Planetary Science Conference, 2140
Straniero, O., Gallino, R., & Cristallo, S. 2006, NuPhA, 777, 311, doi: 10.1016/j.nuclphysa.2005.01.011
Tagliente, G., Milazzo, P. M., Fujii, K., et al. 2008a, PhRvC, 78, 045804, doi: 10.1103/PhysRevC.78.045804
Tagliente, G., Fujii, K., Milazzo, P. M., et al. 2008b, PhRvC, 77, 035802, doi: 10.1103/PhysRevC.77.035802
Tagliente, G., Milazzo, P. M., Fujii, K., et al. 2010, PhRvC, 81, 055801, doi: 10.1103/PhysRevC.81.055801
—. 2011a, PhRvC, 84, 055802, doi: 10.1103/PhysRevC.84.055802
—. 2011b, PhRvC, 84, 015801, doi: 10.1103/PhysRevC.84.015801
—. 2013, PhRvC, 87, 014622, doi: 10.1103/PhysRevC.87.014622
Takahashi, K., & Yokoi, K. 1987, Atomic Data and Nuclear Data Tables, 36, 375, doi: 10.1016/0092-640X(87)90010-6
Trippella, O., Busso, M., Maiorca, E., Käppeler, F., & Palmerini, S. 2014, ApJ, 787, 41, doi: 10.1088/0004-637X/787/1/41

Trippella, O., Busso, M., Palmerini, S., Maiorca, E., & Nucci, M. C. 2016, ApJ, 818, 125, doi: 10.3847/0004-637X/818/2/125

Vescovi, D., Cristallo, S., Busso, M., & Liu, N. 2020, ApJL, 897, L25, doi: 10.3847/2041-8213/ab9fa1

Vescovi, D., Cristallo, S., Palmerini, S., Abia, C., & Busso, M. 2021, A&A, doi: 10.1051/0004-6361/202141173

Vlemmings, W. 2012, IAU Symposium, 283, 176, doi: 10.1017/S1743921312010903

Vlemmings, W. H. T. 2011, in Asymmetric Planetary Nebulae 5 Conference, ed. A. A. Zijlstra, F. Lykou, I. McDonald, & E. Lagadec, 89. https://arxiv.org/abs/1009.4067

Walter, G., Beer, H., Kaeppeler, F., & Penzhorn, R. D. 1986, A&A, 155, 247

Wasserburg, G. J., Boothroyd, A. I., & Sackmann, I. J. 1995, ApJL, 447, L37, doi: 10.1086/309555

Yoon, S. C., Langer, N., & van der Sluys, M. 2004, A&A, 425, 207, doi: 10.1051/0004-6361:20040231

Zinner, E. 1998, Meteoritics and Planetary Science, 33, 549, doi: 10.1111/j.1945-5100.1998.tb01664.x

—. 2014, Presolar Grains, ed. A. M. Davis, Vol. 1, 181–213